Manganese cycling and transport in boreal estuaries impacted by acidic Mn-rich drainage

Yu, CX; Turner, S; Huotari, S; Chen, N; Shchukarev, A; Österholm, P; Lopez-Fernandez, M; Högfors-Rönnholm, E; Sachpazidou, V; Mayanna, S; Hogmalm, KJ; Virtasalo, JJ; Boily, JF; Dopson, M; Astrom, ME

Contents lists available at ScienceDirect

Geochimica et Cosmochimica Acta

journal homepage: www.elsevier.com/locate/gca

Manganese cycling and transport in boreal estuaries impacted by acidic Mn-rich drainage

Changxun Yu [a,*], Stephanie Turner [b,c], Simo Huotari [d], Ning Chen [e], Andrey Shchukarev [f], Peter Österholm [g], Margarita Lopez-Fernandez [b,h], Eva Högfors-Rönnholm [i], Varvara Sachpazidou [b], Sathish Mayanna [j,k], K. Johan Hogmalm [l], Joonas J. Virtasalo [m], Jean-François Boily [f], Mark Dopson [b], Mats E. Åström [a]

[a] Department of Biology and Environmental Science, Linnaeus University, 39231 Kalmar, Sweden
[b] Centre for Ecology and Evolution in Microbial Model Systems (EEMiS), Linnaeus University, 39231 Kalmar, Sweden
[c] Department of Forest Mycology and Plant Pathology, Swedish University of Agricultural Sciences, 75007 Uppsala, Sweden
[d] Department of Physics, University of Helsinki, 00014 Helsinki, Finland
[e] Canadian Light Source, University of Saskatchewan, S7N 0X4 Saskatoon, Canada
[f] Department of Chemistry, Umeå University, 90187 Umeå, Sweden
[g] Åbo Akademi University, Department of Geology and Mineralogy, 20500 Åbo, Finland
[h] Department of Microbiology, University of Granada, 18071 Granada, Spain
[i] Research and Development, Novia University of Applied Sciences, 65200 Vaasa, Finland
[j] German Research Center for Geosciences (GFZ), Telegrafenberg, 14473 Potsdam, Germany
[k] Carl Zeiss Microscopy GmbH, Carl Zeiss Strasse 22, 73447, Oberkochen, Germany
[l] Department of Earth Sciences, University of Gothenburg, 40530 Gothenburg, Sweden
[m] Marine Geology, Geological Survey of Finland (GTK), 02150 Espoo, Finland

ARTICLE INFO

ABSTRACT

As critical transition zones between the land and the sea, estuaries are not only hotspots of hydrogeochemical and microbial processes/reactions, but also play a vital role in processing and transferring terrestrial fluxes of metals and nutrients to the sea. This study focused on three estuaries in the Gulf of Bothnia. All of them experience frequent inputs of acidic and Mn/metal-rich creek waters due to flushing of acid sulfate soils that are widespread in the creek's catchments. Analyzing existing long-term water chemistry data revealed a strong seasonal variation of Mn loads, with the highest values in spring (after snow melt) and autumn (after heavy rains). We sampled surface waters, suspended particulate matter (SPM), and sediments from the estuarine mixing zones and determined the loads and solid-phase speciation of Mn as well as the composition and metabolic potentials of microbial communities. The results showed that the removal, cycling, and lateral transport of Mn were governed by similar phases and processes in the three estuaries. Manganese X-ray absorption spectroscopy data of the SPM suggested that the removal of Mn was regulated by silicates (e.g., biotite), organically complexed Mn(II), and MnOx (dominated by groutite and phyllomanganates). While the fractional amounts of silicate-bound Mn(II) were overall low and constant throughout the estuaries, MnOx was strongly correlated with the Mn loadings of the SPM and thus the main vector for the removal of Mn in the central and outer parts of the estuaries, along with organically complexed Mn(II). Down estuary, both the fractional amounts and average Mn oxidation state of the MnOx phases increased with (i) the total Mn loads on the SPM samples and (ii) the relative abundances of several potential Mn-oxidizing bacteria (*Flavobacterium, Caulobacter, Mycobacterium,* and *Pedobacter*) in the surface waters. These features collectively suggested that the oxidation of Mn, probably mediated by the potential Mn-oxidizing microorganisms, became more extensive and complete towards the central and outer parts of the estuaries. At two sites in the central parts of one estuary, abundant phyllomanganates occurred in the surface sediments, but were converted to surface-sorbed Mn(II) phases at deeper layers (>3–4 cm). The occurrence of phyllomanganates may have suppressed the reduction of sulfate in the surface sediments, pushing down the methane sulfate transition zone that is typically shallow in estuarine sediments. At the outermost site in the estuary, deposited MnOx were reduced immediately at the water–sediment interface and converted most likely to

Mn carbonate. The mobile Mn species produced by the Mn reduction processes (e.g., aqueous Mn(II) and ligand complexed Mn(III)) could partly diffuse into the overlying waters and, together with the estuarine Mn loads carried by the surface waters, transfer large amounts of reactive Mn into open coastal areas and subsequently contribute to Mn shuttling and inter-linked biogeochemical processes over the seafloor. Given the widespread occurrence of acid sulfate soils and other sulfidic geological materials on many coastal plains worldwide, the identified Mn attenuation and transport mechanisms are relevant for many estuaries globally.

1. Introduction

As a highly reactive and biologically important element, manganese (Mn) is crucial in numerous biogeochemical reactions/processes in the global ocean and its marginal seas. The distribution and bioavailability of Mn (an essential micronutrient for phytoplankton) may act as a (co–) limiting factor for primary productivity in some parts of the global ocean, such as the Southern Ocean (Balaguer et al., 2022; Browning et al., 2021). Natural Mn (hydr-)oxides, in particular those whose formation are catalyzed by microbial activities, possess low point of zero charges as well as high chemical reactivities and (oxidative) surface areas (Post, 1999; Tan et al., 2008; Villalobos et al., 2003). The formation and redox-cycling of these (hydr-)oxides could exert a profound impact on the transport, dynamics, and bioavailability of co-occurring macro- and micro-nutrients such as phosphorus (P), nitrogen, and trace metals (Fernandes et al., 2015; Hermans et al., 2019; Lee et al., 2021), which in turn affect the productivity and structure of plankton and benthic communities in the oceanic and coastal ecosystems.

Coastal and shelf sediments, in particular those fed by rivers/creeks with high loadings of reactive Mn, act as the main sources of Mn to the global ocean (Charette et al., 2016; Lenstra et al., 2022; Tessin et al., 2020). The Mn fluxes derived from these sediments are laterally transported seawards, triggering a repeated resuspension/redeposition and associated redox-cycling ("shuttling") of Mn (hydr-)oxides in the bottom waters and/or sediment-mixed layers from continental shelves to deep ocean (Jensen et al., 2020; Jilbert and Slomp, 2013; Lenstra et al., 2019; Lenz et al., 2015; Owings et al., 2021). This process not only strongly affects the cycling of land-derived nutrients (e.g., P) (Dellwig et al., 2010; Jilbert and Slomp, 2013), but can also exert a strong impact on the degradation and processing of organic matter (OM) in the ocean. First, the repeated reduction of Mn (hydr-)oxides is expected to contribute strongly to the anaerobic mineralization of co-cycled OM, as found for surface sediments with (relatively) abundant Mn (hydr-)oxides (Hyun et al., 2017; Jensen et al., 2003; Owings et al., 2021; Thamdrup and Canfield, 1996). Second, increasing evidence shows that Mn (hydr-)oxides can selectively bind and/or oxidize certain organic compounds (Allard et al., 2017; Chorover and Amistadi, 2001; Estes et al., 2016; Johnson et al., 2015; Sunda and Kieber, 1994; Zhang et al., 2021) and thus, act as an important yet poorly-constrained factor influencing the transport, degradation, and storage of sedimentary OM (Jones et al., 2018). Taken together, it is of great importance to advance our knowledge on the mechanisms and pathways whereby Mn is released, transported, and recycled across the land-coast-shelve-ocean continuum, particularly in the regions with large inputs of land-derived Mn fluxes.

In settings where sulfide-bearing calcite-poor sediments are brought into contact with atmospheric O_2 via natural phenomena (e.g., land uplift and droughts) or human activities (e.g., artificial drainage and excavations), the oxidation of sulfide minerals produces large quantities of acidity that severely acidify the soil to pH values typically between 2.5 and 4.0 (Boman et al., 2010; Mosley et al., 2014). This results in the formation of acid sulfate (AS) soil that is widely distributed on many low-lying coastal plains worldwide. It has been estimated that these soils occupy 14–24 million ha around the world (Andriesse and Van Mensvoort, 2006), but the figure is probably considerably higher because (i) regional or nationwide surface-water monitoring programs contain systematic gaps in coastal areas (Destouni et al., 2008) and (ii) the soils are not (or only marginally) enriched in total contents of metals

(including Mn), compared to other minerogenic soils, and thus not easily identified in traditional soil and geochemical mapping (Astrom et al., 2018). In particular, the areal extent, depth penetration, and chemical reactivity of AS soils are expected to increase worldwide, considering that (i) artificial drainage is increasing as a result of increasing demands from growing human populations in coastal regions, and (ii) future climate change will lead to higher air temperatures and more frequent/ prolonged periods of droughts followed by heavy rainfalls, which favors oxidative weathering of sulfide-rich sediments and thus AS soil formation. Under high flow conditions such as heavy rains and snow melting, AS soils discharge large quantities of dissolved Mn (along with other metals) into associated creeks/rivers and recipient estuaries (Astrom et al., 2012; Macdonald et al., 2007; Nystrand et al., 2016; Virtasalo et al., 2020; Yu et al., 2016). For instance, during a 4-day rainfall event, AS soil floodplains in two small catchments (occupying 5.2 km^2 and 4.5 km^2) exported approximately 83 kg and 63 kg Mn, respectively, into the Tweed River on the eastern coast of Australia (Macdonald et al., 2007), and in a boreal catchment of 223 km^2 with a large share of AS soils exported 110 tons Mn annually into the recipient estuary (Nordmyr et al., 2008a). Consequently, AS soils supply large amounts of reactive Mn to many estuaries and inter-connected coastal zones worldwide, thereby exerting long-term and far-reaching impacts on the ecosystem health/services and carbon/nutrient cycling in these ecosystems.

The formation pathways and chemical/structural characteristics of biogenic Mn hydroxides have been extensively investigated using cultivated Mn(II)-oxidizing organisms (bacteria, fungi, and algae) under controlled physicochemical conditions (Chaput et al., 2019; Hansel et al., 2012; Learman et al., 2011; Santelli et al., 2011; Saratovsky et al., 2009; Webb, 2005; Webb et al., 2005; Yu et al., 2012; Zhang et al., 2019). Considering the diversity of Mn(II)-oxidizing organisms and their complex interactions with other organisms and environmental parameters under natural conditions, particularly in Mn-rich systems (Carmichael et al., 2013a; Chaput et al., 2015; Santelli et al., 2014; Santelli et al., 2010; Sjöberg et al., 2020), the results obtained by these studies are not directly applicable to natural environments, such as the AS soil impacted estuaries. Spatiotemporal variations in the environmental parameters like salinity, pH, temperature, nutrients, and quality of dissolved OM could strongly affect the survival, viability, and structure of microbial communities (Nichols et al., 1999; Zhou et al., 2022). In particular, salinity and pH vary widely over temporal and spatial scales along the mixing zone of the AS soil impacted estuaries (Astrom et al., 2012; Nordmyr et al., 2008a). Therefore, these estuaries can serve as natural "experimental bioreactors" for investigating how (i) Mn(II)-oxidizing microorganisms and linked microbial communities respond to environmental factors and catalyze Mn(II) oxidation and (ii) Mn (hydr-)oxides as Mn oxidation products are ultimately formed and, in combination with other processes, regulate estuarine behavior and seaward transport of Mn.

Molecular-level knowledge on the key phases, processes, and pathways governing Mn removal, recycling, and seaward transport in AS soil impacted estuaries is still lacking. To fill this knowledge gap, we conducted a systematic field-based study on three AS-soil impacted creeks (Vörå, Munsala, and Toby) and associated estuaries in the Boreal zone. The overall objectives were to (i) explore how environmental factors and microbial communities interact and mediate Mn oxidation (and subsequent formation of Mn (hydr-)oxides) in the water columns and drive Mn redox-cycling and linked early-diagenetic processes in the surface

sediments along the estuarine mixing zones and (ii) elucidate the key mechanistic and biogeochemical processes that control input, removal, recycling, and lateral transport of Mn within the water columns and surface sediments in the estuarine systems. The results have broad implications for unravelling the key biogeochemical Mn processes in AS-soil impacted estuaries and for assessing their contributions to Mn shuttling/fluxes across the estuary-coastal-open sea continuum in these regions.

2. Study areas

The three studied creeks (Vörå, Munsala, and Toby) are located within an approximately 70-km long stretch of the western Finland coastline (Fig. 1a). The catchments of these creeks are underlain by Proterozoic granitoids and gneisses, largely covered by unconsolidated glacial till that supports forest and mires (Astrom et al., 2010). To increase forest productivity, the forested areas have been largely drained by open surface drains (60–80 cm deep), mainly in the 1960s and 1970s (Finnish Field Drainage Center, 2001). In a large part of the valleys and depressional areas in these catchments several meters thick fine-grained brackish-water sediments exist. They were formed on the seafloor in the Holocene and now occur in the terrestrial landscape as a result of postglacial isostatic land uplift (Mäkinen and Saaranen, 1998). These sediments typically contain 0.2–2.0 % reduced sulfur in the form of pyrite and metastable iron sulfides (Astrom and Björklund, 1997; Boman et al., 2010) and have been drained since the early 19th century to generate agricultural land, initially by manual ditching and over the last few decades by subsurface (drainpipe) techniques (Astrom et al., 2010). These human activities increased exposure of the iron sulfides to atmospheric oxygen, turning the sediments to AS soils that periodically discharged very acidic and Mn(/metal)-rich drainages (Astrom and Björklund, 1995; Yli-Halla, 1997). The catchments of the three creeks are sparsely populated, with no lake basin and only a minor influence of industrial and urban effluents (Rautio and Ilvessalo, 1998).

The estuaries of the three creeks are shallow, non-tidal, and well-sheltered from wave action by the surrounding land area and islands (Fig. 1b-d). However, the water levels in the estuaries can fluctuate by approximately ± 1 m (Nordmyr et al., 2008b; Virtasalo et al., 2020) due to variations in wind and atmospheric pressure. The pH, electric conductivity (EC), and other physiochemical variables fluctuate significantly along the estuarine mixing zones, depending mainly on the extent of input of fresh waters from the creeks that are frequently acidified.

Generally, these creeks have the highest water flows in late spring and autumn, during which a large amount of snowmelt or rainwater, respectively, is discharged from the catchments, including acidic waters from AS soils under the farmlands. The estuaries and catchments are covered by ice and snow annually from December to April/May while the annual mean temperature and precipitation of this region is approximately 3 °C and 500 mm, respectively.

3. Materials and Methods

3.1. Sampling and field measurements

Water sampling was carried out in late May 2017 and early May 2018 (after the snow melt) from the Vörå creek outlet and estuary (four estuarine sites, Fig. 1b) and on one occasion in early May 2018 from the other two creek outlets and estuaries (three estuarine sites in each; Fig. 1c-d). Temperature (T), pH, electrical conductivity (EC), oxidation–reduction potential (ORP), and concentrations of Cl^-, NH_4^+, and NO_3^- were measured on-site with a Eureka Environmental Manta 2 Multiprobe. Two water samples were collected from each sampling site using sterilized glass bottles and acid-washed polyethylene bottles for microbial and chemical analyses, respectively. The waters sampled with sterilized glass bottles were transported back to the laboratory in an ice box, immediately filtered through 0.1 μm (Durapore, PVDF membrane, Merck Millipore) sterilized filters, and frozen at −80° C, while a portion for later observations with scanning electron microscopy (SEM) were air-dried. The waters in polyethylene bottles were split in two portions, one was filtered through 0.1 μm membrane (Durapore, PVDF membrane) before being acidified to pH < 2 with ultrapure HNO_3 for determining the concentrations of dissolved plus colloidal fractions (hereafter collectively referred to as the "<0.1 μm fraction") of cations and metals while the second bottle was untreated for analyzing the concentrations of total and dissolved organic carbon. In addition, one portion of the waters collected from the Vörå creek and its estuary during the 2017 campaign was unfiltered and acidified to pH < 2 with ultrapure HNO_3 for measuring the "total acid-available" fraction of cations and metals. The differences between "total acid-available" and "<0.1 μm fraction" mainly included colloids with sizes larger than 0.1 μm and part of the particulate phase that can easily be dissolved under acidic conditions (hereafter referred to as ">0.1 μm fraction"). Furthermore, approximately 12 L of surface water was collected from the outermost three sites in the estuaries using clean plastic buckets and
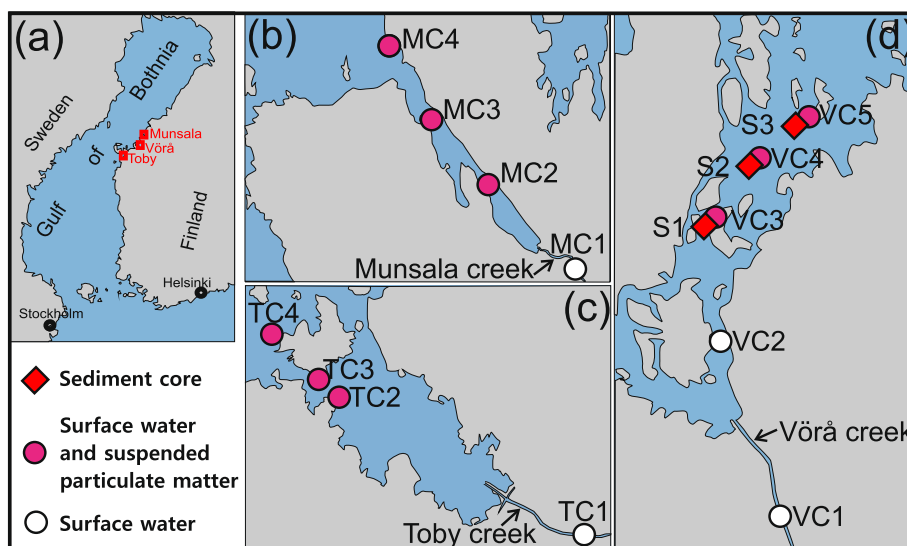

Fig. 1. Locations of the three studied creeks (a, marked as red squares) as well as the sampling sites in each of the creeks and their estuaries (b-d). Water quality was regularly monitored by the Finnish Environment Institute (SYKE) during the last 50–60 years close to sites TC1 and VC1.

subsequent centrifugation (*12000 × g,* 20 min) was applied to obtain the suspended particulate matter (SPM) from these waters.

Approximately 40 cm long sediment cores were sampled in August 2018 from three sites (S1- S3; Fig. 1d) in the outer part of the Vörå estuary using a KC Kajak sediment core sampler. The upper 20 cm of the sediment cores, where sediment color changed from yellowish/brownish to black (Fig. S1), were sectioned in the field (via pushing the sediment cores upwards) at every 2 cm interval from the surface to 10 cm and every 5 cm at 10 to 20 cm depth. Three subsamples were obtained from each depth interval for Mn XAS plus microbial and chemical analyses. The oxidation of air-sensitive species was minimized by filling 15 mL Falcon tubes with sediment, after which the capped tubes were wrapped with parafilm and transported in an ice box. The black color of the subsurface sediments, caused by fine-grained (clay and silt sized) metastable iron sulfides (Boman et al., 2008), did not change during sampling and transport, indicating that the sediments remained fully reduced during handling. Thereafter, the subsamples for Mn XAS and microbial analyses were kept frozen at −80 ℃ until further treatment/analyses.

3.2. Chemical, bulk density, and LOI analyses

Subsamples of air-dried and pulverized sediment and SPM samples (including blind replicates) were randomized and subjected to a near-total four-acid (HF + HClO$_4$ + HNO$_3$ + HCl) digestion in an accredited laboratory. The concentrations of Mn, Fe, Al, and S in all resulting solutions were determined by inductively coupled plasma optical emission spectrometry (ICP-OES) using the SFS-EN ISO 11885 standard method. The precision calculated based on repeated analyses of blind replicates was better than 7 %. Certified reference materials were employed for quality control of the analyses. The sediment samples were also analyzed for dry bulk density (DBD, in kg/m^3) by drying subsamples of known volumes at 105 °C overnight and weight loss on ignition (LOI) by ashing at 550 °C in a furnace for 4 h.

The concentrations of Mn, Fe, Al, S, P, K, Na, Mg, and Ca in both unfiltered and filtered (<0.1 μm) water samples collected in 2017 were analyzed on an Agilent 7500 ICP-MS. Drift and accuracy were monitored by analysis of dissolved rock standards of granite (SARM 48) and basalt (W-1). The relative standard deviation of triplicate measurements was within 10–12 %. The concentrations of the same elements in filtered water samples collected in 2018 were determined on an ICP-OES at an accredited laboratory following the standard method SFS-EN ISO 11885. The concentrations of dissolved organic carbon (DOC) in the unfiltered water samples were determined by a TOC-5000A analyzer (Shimadzu Corporation) at an accredited laboratory according to the European standard method EN 1484 (EN, 1997).

3.3. DNA extraction, PCR amplification, sequencing, and microbial community analyses

DNA was extracted from the 0.1 μm filters (surface water samples) and sediment samples (Tables S1 and S2), a portion of the 16S rRNA gene PCR amplified, and the products prepared for sequencing as previously described (Seidel et al., 2022). Briefly, between 100 and 800 mL surface water (Table S1) and 250 mg sediment were used to extract DNA using the QIAGEN DNeasy PowerWater and PowerSoil kits for the water and sediment samples, respectively. Three extraction controls (no filter added) were included and extracted with the QIAGEN DNeasy Power-Water kit to check for contaminants. PCR amplification of the 16S rRNA gene V3-V4 region used primers 341F and 805R (Hugerth et al., 2014) and the quality and quantity of the PCR products were checked using gel electrophoresis and Qubit® 2.0 Fluorometer (Invitrogen), respectively. Although the extraction controls showed no detectable DNA (i.e., < 0.05 ng μL^{-1}, Table S1) and could not be amplified successfully, they were sent for sequencing. Illumina library preparation and subsequent sequencing was performed by the Science for Life Laboratory

(SciLifeLab), Stockholm on the Illumina MiSeq platform generating 2 × 301 bp pair-end reads. The raw 16S rRNA gene amplicon sequences are available at NCBI Sequence Read Archive (SRA) under the BioProject ID PRJNA977650.

The bacterial 16S rRNA gene reads were analyzed using the version 2.2.0 of the Ampliseq pipeline (Straub et al., 2020) that incorporates FastQC (v. 0.11.9), Cutadapt (v. 3.4), DADA2 (v. 1.22.0) to generate amplicon sequence variants (ASVs), and classification against the SILVA database (v. 138.1). Computations were carried out using resources at the Uppsala Multidisciplinary Center for Advanced Computational Science, UPPMAX and data processing was performed in R Studio version 3.6.3 (R Core Team, 2019) with the vegan package (Oksanen et al., 2019). The ASVs identified in the extraction controls were removed from all samples and ASVs classified as chloroplasts or mitochondria were filtered out. Beta diversity of water and sediment microbial communities was visualized by a non-metric multidimensional scaling (NMDS) based on a Bray Curtis dissimilarity matrix using relative ASV abundances. Water sample environmental parameters were plotted on the NMDS using the envfit function from vegan. To identify genera that are potentially involved in manganese oxidation or reduction, a list was compiled based on a literature search (Table S3). Finally, PICRUSt2 software v. 2.5.0 was used to predict functional gene frequencies from the relative proportions of the 16S rRNA gene frequencies (Douglas et al., 2020) based on KO (KEGG orthology) identifiers. From the 33,625 input ASVs, 0.13 % could not be aligned to the reference database and 6.5 % were excluded due to a NSTI (nearest-sequenced taxon index) value higher than 2. The average weighted NSTI across all samples was rather high with a value of 0.26 indicating the microbial communities were quite dissimilar from the reference sequences, therefore the predictions should be interpreted with caution. The output was searched for genes of interest (Table S4) that were either related to Mn cycling or potentially associated pathways. Predictions of the functional potential of a microbial community based on marker gene sequencing comes with several limitations (Douglas et al., 2020), e.g., their bias towards available reference genomes and the used databases as well as the insufficient resolution to reveal strain-specific differences in functionality with the latter also applying to the abovementioned genera-based analysis.

3.4. Cryogenic X-ray photoelectron spectroscopy (XPS)

Wet pastes of selected SPM samples were analyzed for surface chemical and elemental composition using cryogenic XPS by following a precooling procedure that preserved the samples at −150 °C during the course of the measurements (Ramstedt et al., 2004; Shchukarev et al., 2007). This procedure retained water in the samples and minimized changes in the oxidation state of the metal ions on the surfaces of the minerals. Measurements were performed with a Kratos Axis Ultra DLD electron spectrometer using a monochromated Al Kα source operated at 150 W, a hybrid lens system with magnetic lens providing an analysis area of 0.3 × 0.7 mm^2, and a charge neutralizer. Survey spectra (1100 eV to 0 eV) were collected using a pass energy of 160 eV, while high-resolution spectra were recorded with a pass energy of 20 eV for individual photoelectron lines of all detected elements (C1s, N1s, O1s, F1s, Ca2p, Mg2p, Fe2p, Mn2p, Si2p, Al2p, and Cl2p). The XPS spectra were analyzed using the CasaXPS software package (Fairley, 2009). All spectra were subtracted with a Shirley background and charge-referenced to the C 1 s peak of the adventitious carbon at 285.0 eV. The atomic concentrations of all detected elements were quantified based on integrated areas of corresponding peaks and their associated elemental sensitivity factors. High-resolution spectra for C1s, N1s, O1s, Fe2p3/2, Mn2p, Si2p, and Al2p were deconvoluted into different peaks using a linear combination of 70:30 G-Lorentz functions (for details, see SM-1).

3.5. Mn K-edge X-ray absorption spectroscopy (XAS)

Mn K-edge XAS spectra of air-dried and finely pulverized SPM samples (with different Mn-loadings and locations within the three estuarine mixing zones) were recorded on the Hard X-ray Micro-Analysis (HXMA) Beamline at the Canadian Light Source (Saskatoon, Canada). Throughout the reported Mn XAS experiment, the beamline was configured under its focused operation mode with monochromator Si (1 1 1) crystal and Rh collimating and toroidal mirrors in the X-ray beam path. The samples were packed into Teflon holders, sealed with Kapton tape on both sides, and positioned at approximately 45 degrees to the incident X-ray beam to maximize the fluorescence yield. To reduce the high harmonic components in the incident X-ray beam, the second monochromator crystal was detuned by 50 % at the end of the scan. The spectra were collected in fluorescence mode using a 32 element Ge detector, with different scan steps for the pre-edge (-200 ~ -30 eV; 5 eV/step), XANES (-30 ~ 50 eV; 0.25 eV/step), and EXAFS (50 eV ~ 11.5 Å-1; 0.05 Å^{-1}/step), respectively. To achieve satisfactory signal-to-noise ratios, two to four scans were recorded for each sample. Internal calibration for each individual scan was performed upon simultaneously recorded XAS spectrum of a Mn metal foil from Exafs Materials (https://exafsmaterials.com/) in transmission mode.

Portions of sediment samples from the upper 10 cm were dried under oxygen-free conditions in a glove box and finely pulverized with an agate mortar and pestle. XANES spectra of a total of thirteen sediment samples and EXAFS spectrum of the uppermost sediment sample at site S2 were recorded on a laboratory-based X-ray absorption spectrometer (the HelXAS beamline, Center for X-ray Spectroscopy, University of Helsinki) using a Rowland-circle spectrometer in the Johann geometry (Honkanen et al., 2019). The Bremsstrahlung from an Ag-anode water-cooled x-ray tube was monochromated by a Si(4 4 0) spherically bent analyzer crystal with a bending radius R = 0.5 m. The X-ray tube was run with 20 mA and 15 kV to optimize the count rate and contribution from monochromator harmonics. The detector was a Si drift diode. The samples were fixed in steel gaskets, encapsulated from both sides with an adhesive tape, and placed in the beam at the exit window of the X-ray tube. The integration time depended on the signal and was optimized such that the statistical noise of each spectrum was the same order of magnitude. The spectra (6517–6617 eV, with a step size of 0.5 eV) were measured with and without sample to obtain the I and I0 for Beer-Lambert law: mu = ln(I0/I), and stray scattering background was subtracted from both I and I0 before taking the logarithm.

To aid the interpretation of the sample XANES/EXAFS spectra, a range of Mn reference minerals/phases were purchased or synthesized (see SM-2 for details). The references included biotite, chlorite, rhodochrosite ($MnCO_3$), manganese sulfide (MnS), Mn(II)-sorbed on humic acid (Mn(II)-HA), hausmannite (Mn_3O_4), groutite (α-MOOH), manganite (γ-MnOOH), bixbyite (Mn_2O_3), triclinic birnessite, hexagonal birnessite, and vernadite. Mn XAS spectra of these references were recorded from −150 to + 190/570 eV (relative to the Mn K-edge) using a fly scan mode with a 0.5 eV step and an acquisition time of 0.5 s per step at the Balder beamline of the MAX IV laboratory (Lund, Sweden). The spectra of biotite, chlorite, and Mn(II)-HA were collected in fluorescence mode while the other references were mixed with polyethylene and analyzed in transmission mode. Between six and fifteen scans were recorded and merged to increase the signal-to-noise ratio. In addition, XAS spectra of Mn(II)-HA, rhodochrosite, groutite, manganite, manganese sulfide, triclinic birnessite, hexagonal birnessite, and vernadite were collected at the HelXAS beamline using the same experimental set-up as for the sediment samples. Additional reference spectra included $MnPO_4$ (Manceau et al., 2012), feitknechtite (β-MnOOH) (Manceau et al., 2012), aqueous Mn(II) (Yu et al., 2016), and Mn(II)-sorbed fungi (Grangeon et al., 2010). These reference spectra represented a wide range of Mn chemical/coordination environments (Table S5) that could potentially occur in the SPM and sediment samples.

Manganese XAS scans of each sample and reference were energy-calibrated, merged, and normalized following standard procedures in the software Athena (Ravel and Newville, 2005). EXAFS spectra were extracted from the normalized data using a cubic spline function. The solid-phase speciation of Mn in the SPM samples was quantified via fitting each sample XANES spectrum with a linear combination of the reference spectra using two methods. In method one, each sample spectrum was fitted by a sum of all reference spectra without any constraints. References with negative weights were progressively eliminated in ascending order of their weights (when one reference was eliminated, the fitted weights of the others also changed). After eliminating all references with negative weights, each was re-included randomly one-by-one in the fit to ensure that the global minimum was reached. For method two, the fitting was started with the reference spectrum giving the lowest R-factor. Additional reference spectra were added stepwise if the R-factor decreased > 10 % relative to the previous fit. In the fitting, the weights of all references were constrained to be positive and the sum of their weights was not forced to unity. Both methods have been used to gain quantitative information on Mn valence and speciation in various natural and experimental samples (Bargar, 2005; Flynn and Catalano, 2019; Herndon et al., 2014; Leven et al., 2018; Liu et al., 2021b; Manceau et al., 2012; Santelli et al., 2011; Wu et al., 2020). Since the reference spectra were collected using different set-up (e.g., energy resolution) than the spectra of SPM samples, the results of the LCF-XANES analysis should be interpreted with caution.

The EXAFS spectra of the SPM samples and selected references (including aqueous Mn(II), Mn(II)-HA, triclinic birnessite, and vernadite that were estimated to occur in the SPM samples by the LCF-XANES analysis) were k^3-weighted and converted to R-space by Fourier transform (FT) over the k range of 2.0 to 10.2–11.5 Å (depending on data quality) using a Hanning window. The EXAFS spectra were fitted by non-linear least-square methods in R-space using the Artemis program (Ravel and Newville, 2005). Details of the EXAFS fitting are given in SM-3.

3.6. Scanning electron microscopy (SEM)-energy dispersive spectrometry (EDS) analyses

The solid materials (trapped by 0.1 μm filters) isolated from three surface waters (VC2 May-18, TC2 May-18, and TC4 May-18) collected in 2018 were air-dried (and uncoated) for SEM-EDS investigations, for determining the elemental compositions of mineral assemblages and visualizing the morphological features of microbial cells/biofilms that are resistant to dehydration. The analyses were carried out in low vacuum mode on a Field Emission-Scanning Electron Microscope (Zeiss Ultra Plus) at the GFZ German Research Centre for Geosciences, Potsdam, Germany. Elemental analysis on specific spots was performed using a Thermo Scientific EDS detector at an acceleration voltage of 5 to 20 kV with a 30 μm aperture size. The EDS elemental counts were background- and ZAF-corrected. Since the filters were carbon-based, the EDS results of carbon should be interpreted with care.

3.7. Long-term water monitoring data

In the 1960 s, the Finnish Environment Institute (SYKE) started monitoring the water quality at sites VC1 and TC1 (Fig. 1c, d) approximately every one to three months and stored the data in the open database HERTTA. The long-term series data for pH, EC, and concentrations of Mn, Al, and sulfate were downloaded from the database and included in this study. The measurements of pH and EC were carried out on site with pre-calibrated pH/EC sensors, while the concentrations of Mn, Al, and sulfate in surface waters (filtered through 0.45 μm membranes) were analyzed at accredited laboratories (e.g., AHMA Ympäristo Oy., Etelä-Pohjanmaan ELY-keskus Oy, Eurofins Environment Testing Finland Oy.) using standard methods specified by the Finnish Standards Association and certified by the Finnish Accreditation Service (Yaraghi et al., 2020).

4. Results

4.1. Geochemistry

4.1.1. Creek waters

The concentration of dissolved (<0.45 μm) Mn at the outlets of the Vörå and Toby creeks varied by nearly three orders of magnitude during the last 50–60 years and spanned from 69 to 3700 μg/L and from 50 to 3300 μg/L, respectively (Fig. 2). When aggregated monthly over the whole monitoring period, the Mn concentrations for these two creeks fluctuated almost synchronously and overall peaked in spring (March and April) and autumn (October and November; Fig. 3). The Mn concentrations for these two creeks also displayed similar co-variations with pH and EC as well as the concentrations of sulfate and dissolved Al (Fig. 2).

On the occasions when the three creeks were sampled in this study (May 2017 and 2018), the pH of the surface waters at the creek outlets were 4.8–5.8 (Fig. 4a, Table S6) and loaded with 300–567 μg/L dissolved (<0.1 μm) Mn compared to 13 μg/L Mn in the > 0.1 μm fraction measured during the 2017 sampling campaign (Fig. 4b, Table S6). In contrast, the > 0.1 μm fraction of Al and Fe was much more abundant and occurred in higher or similar concentrations as the dissolved fractions (Fig. 4b, Table S6).

4.1.2. Estuarine waters

Along the transects (estuarine mixing zones) from the creek outlets to the outer estuaries, there was an overall increase in both EC and pH (Fig. 4a, Table S6) due to successive in-mixing of brackish seawater. The

concentrations of the > 0.1 μm fractions of Fe (454–886 μg/L) and Al (117–318 μg/L) strongly dominated the "total acid-available" loads of these two metals in the estuarine waters, and gradually decreased along the estuarine mixing zones (Fig. 4b, Table S6). The < 0.1 μm fraction of these two metals also overall decreased down estuary. In contrast, the < 0.1 μm Mn fraction was considerably larger than the > 0.1 μm fraction and decreased at much slower rates in the inner estuaries and further out (Fig. 4b, Table S6). Although the > 0.1 μm Mn fraction remained consistently low throughout the estuarine mixing zones, it accounted for an increasing down estuary share of the total acid-available load.

4.1.3. Estuarine suspended particulate matter

The concentrations of Fe and Al in the SPM samples showed an overall decreasing trend down estuary (Fig. 4b). In contrast, the concentrations of Mn in these samples overall increased down estuary, reaching up to 0.44–0.52 % at the outermost sites (Fig. 4b). Cryo-XPS analyses revealed that the composition of the outermost layers of the frozen wet (without being dried) SPM samples were dominated by C- and O-bearing compounds (Table 1, Fig. S2). From the C1s region of the spectra, C was predominantly associated with aliphatic and aromatic organic compounds followed by carbohydrates and amines (see SM-1 for details, Fig. S3). From the O1s region, O was mainly from water, organic material, and silicate minerals (SM-1, Fig. S3). The concentrations of Mn varied from < 0.1 % (the detection limit of XPS) to 0.22 % (Table 1) and, assuming that the samples contained 90 % water that is typical for surface sediments in the estuary (Yu et al., 2015), the dry-weight concentrations would be approximately 10 times higher than the measured. The concentrations were thus an order of magnitude higher than those
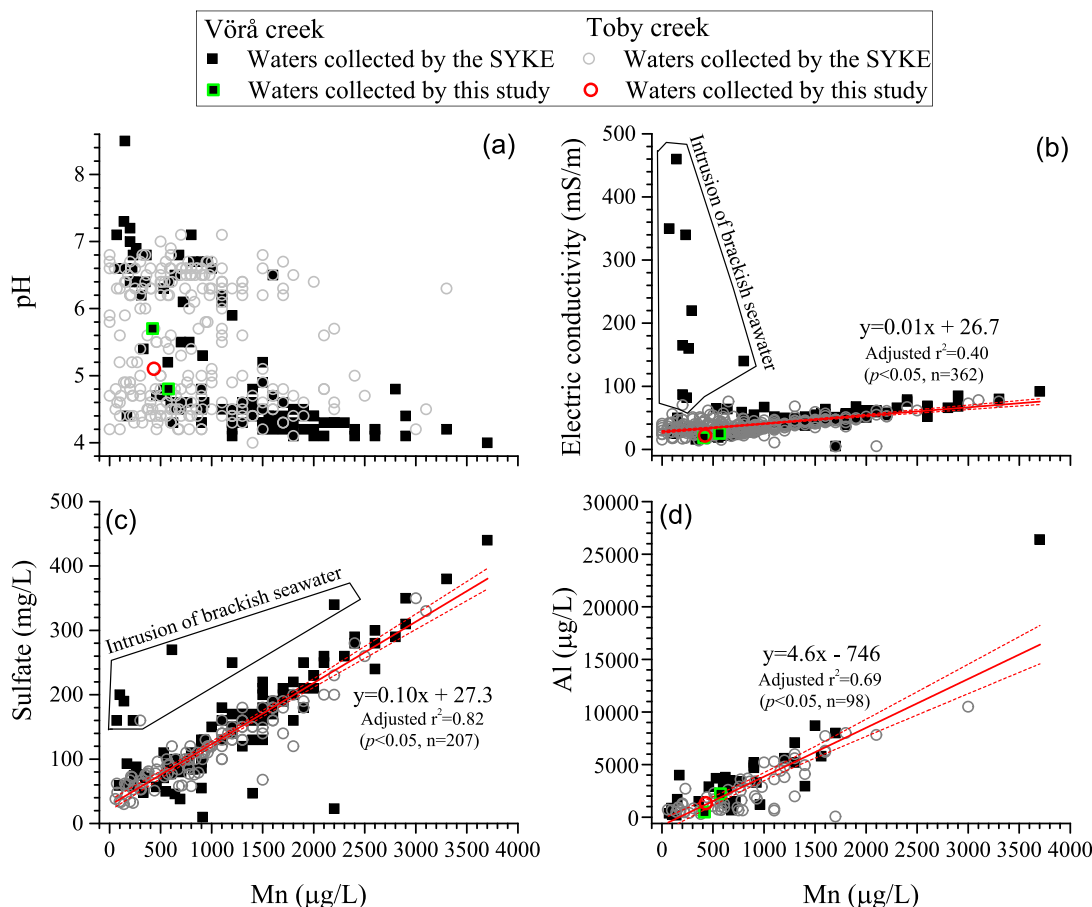
Fig. 2. Manganese concentrations versus pH (a), electric conductivity (b), plus the concentrations of sulfate (c) and Al (d) for the surface waters at the outlets of the Vörå and Toby creeks. The red solid lines are the best linear fits, while the dashed read lines represent 95 % confidence interval. The water samples affected by the intrusion of brackish seawater (marked in b and c) were not included in the linear regression.
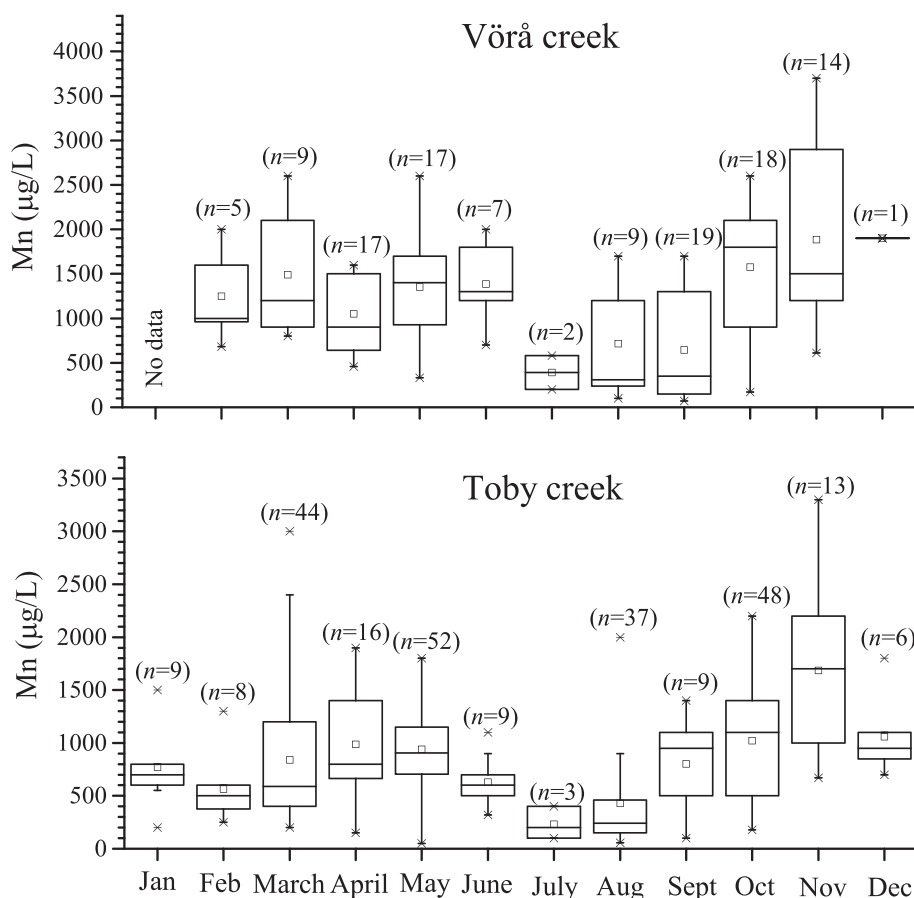
Fig. 3. Boxplots showing the monthly variations in Mn concentrations in the surface waters sampled from the outlets of the Vörå and Toby creeks by the Finnish Environment Institute (SYKE) over the last 50–60 years. Rectangles: 25 % and 75 % quantiles; lines within rectangles: medians; extensions from rectangles: minimums and maximums; squares: mean values; crosses: outlier. The number of water samples is given in the parentheses.

measured on the dried (bulk) SPM samples. This means that the outermost layers of the SPM samples, although being loaded with relatively low amounts of Mn, were still clearly enriched in Mn relative to the bulk samples. The atomic ratios of Mn to Fe and Mn to Al at the outermost layers of the three wet SPM samples where Mn was detected (VC3$_{May.17}$, VC5$_{May.17}$, and VC3$_{May.18}$) varied between 0.14 and 0.31 and 0.03–0.07 (Table 1), respectively. The ratios were thus approximately 3–6 and 2–3 times higher than the corresponding ratios in the same bulk SPM samples. This pointed to a preferential enrichment of Mn relative to Fe and Al in the outermost layers of the SPM.

High-resolution Mn2p XPS spectra of the VC3$_{May.17}$, VC5$_{May.17}$, and VC3$_{May.18}$ SPM samples exhibited two major sub-peaks at ~ 642 eV and ~ 654 eV, corresponding to the Mn2p3/2 and Mn2p1/2 photoelectron lines, respectively (Fig. 5a). The shape and position of these two subpeaks more closely matched with those for MnCl$_2$ than with those for MnOOH and MnO$_2$ (Fig. 5). These spectral features suggest that a majority of Mn at the surface of these samples occurred as the + II oxidation state. Since the Mn loadings on these samples were too low to produce Mn 3 s and Mn 3p spectra of sufficiently high signal-to-noise ratio, we could not further verify this.

High-resolution Fe2p3/2 spectra obtained for VC3$_{May.17}$ and VC5$_{May.17}$ can be deconvoluted into two major components that center around 711–712 eV (49.7–84.2 %) and 714–715 eV (15.8–36.1 %), respectively (Fig. S4a,b). As these energies were in good agreement with those reported for surface Fe(III)-O/OH species on Fe hydroxides and clay minerals (Liu et al., 2019; Yuan et al., 2018), these two components most likely reflected strong contributions of Fe hydroxides or Fe(III) bound to clays on the surface of these two SPM samples. The Fe2p3/2 spectra of VC3$_{May.17}$ also displayed a weak shoulder at ~ 709.4 eV (14.2

%), mostly likely attributed to a small contribution of Fe(II)-O species as found for clay minerals and microbially reduced Fe hydroxides (Liu et al., 2019; Yuan et al., 2018). High-resolution spectra of Al2p and Si2p for these two SPM samples only exhibited a narrow and sharp peak (centering around 74.8 eV and 103.3 eV, respectively; Fig. S4 c-d), which was interpreted to reflect a strong predominance of Al-OH and Si-O components on the surfaces of these samples (see SM-1). The atomic C to N ratios on the surfaces of the fresh SPM samples varied from 12.6 and 28.5 (Table 1), matching with the ratios reported for terrestrial OM from this region (Mattsson et al., 2015). In line with these results, over 80 % N at surfaces of the two SPM samples (VC3$_{May.17}$ and VC5$_{May.17}$) was modelled to be associated with organic C, via a single C-N bond within amide functional group (SM-1, Fig. S3).

To facilitate the observations of how Mn oxidation state and coordination environment in the bulk SPM samples varied as a function of their Mn loadings, the Mn K-edge XANES and EXAFS spectra of SPM samples were organized by the total Mn loadings and compared with those of relevant references (Fig. 6a, 7). The XANES spectra of the two silicate references (biotite and chlorite) displayed four distinct features, including a weak shoulder on edge jump (6548 eV) and an intensive double peak white line (6552 eV and 6557 eV) on the main absorption edge as well as a weak and broad post-edge peak (6570 eV) (Fig. 6a). The shoulder and last two peaks were not present in the spectra of the nonsilicate phases and thus, can be used as reliable spectral "fingerprints" of silicate-bound Mn in the SPM samples. These fingerprint features were clearly resolved in the XANES spectra of the four SPM samples with the lowest Mn loadings (≤0.12 %), indicating large fractional amounts of silicate-bound Mn in these Mn-poor samples. With increasing Mn loadings, these fingerprint features gradually became weaker or even non-
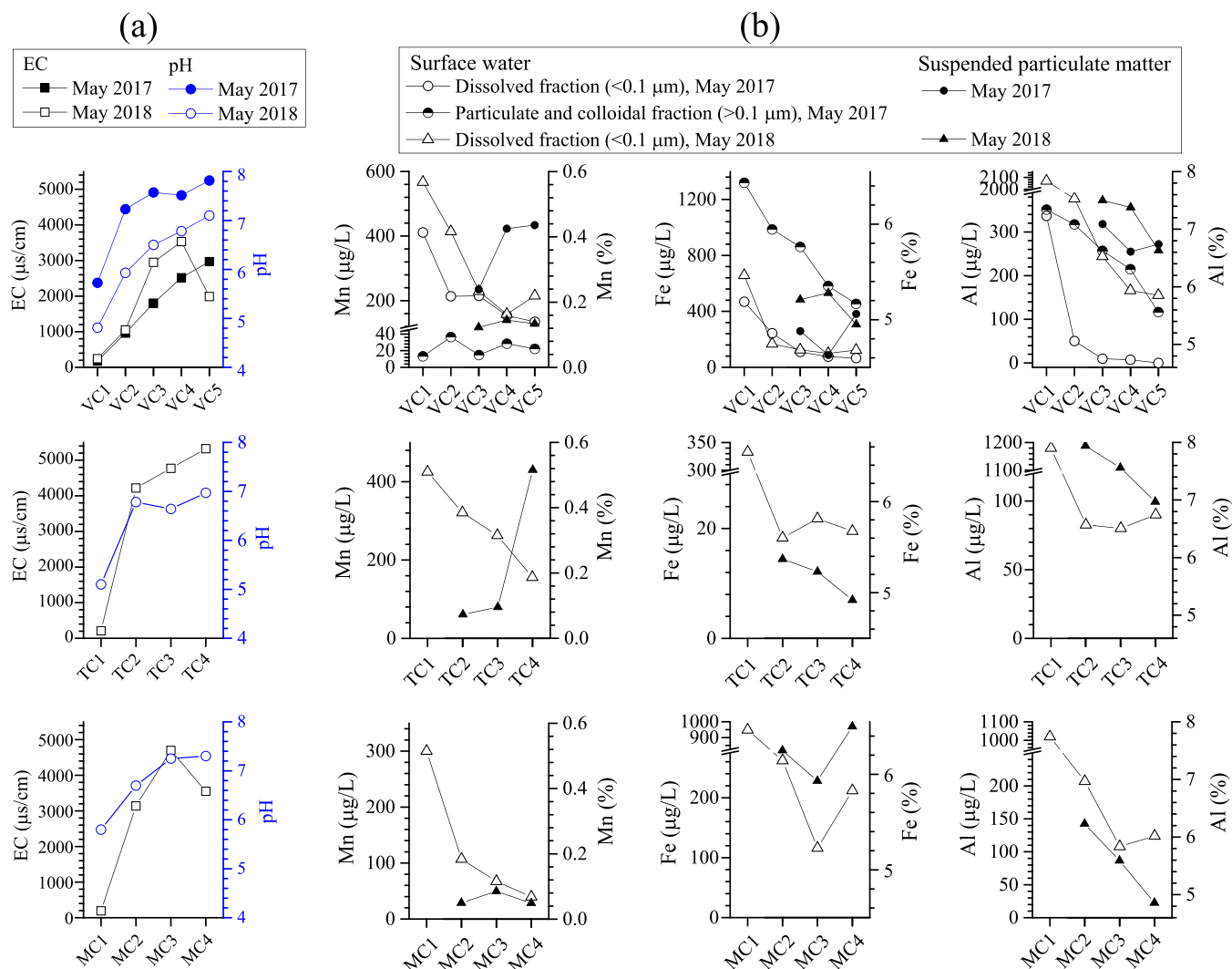
Fig. 4. Changes in pH and electric conductivity (EC) along the transects from the outlets of the creeks (VC1, TC1, and MC1) and to the outer estuaries (a), and in the concentrations of Mn, Fe, and Al in the two size fractions of surface waters and suspended particulate matter (b).

Table 1
Surface composition (in atomic %) of selected SPM samples determined by cryogenic XPS.

	VC3$_{May-17}$	VC5$_{May-17}$	VC3$_{May-18}$	VC4$_{May-18}$	VC5$_{May-18}$	TC2$_{May-18}$	TC3$_{May-18}$	MC2$_{May-18}$	MC3$_{May-18}$
Na %	0.35	0.39	0.40	0.50	0.30	0.80	0.70	0.50	0.90
Ca + Mg %	0.34	0.38	0.40	0.40	0.40	0.50	0.50	0.50	0.50
Cl %	0.13	0.20	0.30	0.40	0.20	0.30	0.50	0.30	0.90
Fe %	0.62	0.71	0.80	1.0	0.90	1.4	1.4	1.5	1.2
Mn %	0.16	0.22	0.11	bdl	bdl	bdl	bdl	bdl	bdl
O %	43.1	45.9	46.7	48.2	51.6	55.4	53.3	49.6	44.0
N %	2.4	2.4	1.7	1.7	2.2	2.3	2.0	2.3	3.2
C %	45.8	42.8	43.8	41.8	38	28.9	31.7	38.9	43.8
Si %	3.6	3.9	1.9	2.3	2.6	5.6	5.3	3.1	3.6
Al %	3.5	3.1	3.8	3.7	3.8	4.9	4.5	3.2	1.9
F %	bdl	bdl	0.1	bdl	0.1	bdl	0.2	bdl	bdl
Sum %	100.0	100.0	100.0	100.0	100.1	100.1	100.1	99.9	100.0
Mn/Fe ratio	0.26	0.31	0.14						
Mn/Al ratio	0.05	0.07	0.03						
C/N ratio	18.9	18.2	25.8	24.6	17.3	12.6	15.9	16.9	13.7

bdl: below the detection limit of XPS, which is approximately 0.1%.

observable. In contrast, the peak at 6552 eV remained almost unchanged and therefore, appeared as a single and dominating peak on the main edge in the XANES spectra of the SPM samples with high Mn loadings (≥ 0.24 %). The energy position of this peak matched well with those of the main absorption peak for the aqueous Mn(II) and Mn(II)-HA

references. These features collectively indicated that (i) the SPM samples were also loaded with abundant non-silicate Mn(II) species (most likely as aqueous Mn(II) and Mn(II)-HA) and (ii) in contrast to silicate-bound Mn, the fractional amounts of these Mn species increased overall with increasing Mn loadings. The spectra of TC4$_{May-18}$ and VC4 $_{May-17}$ with
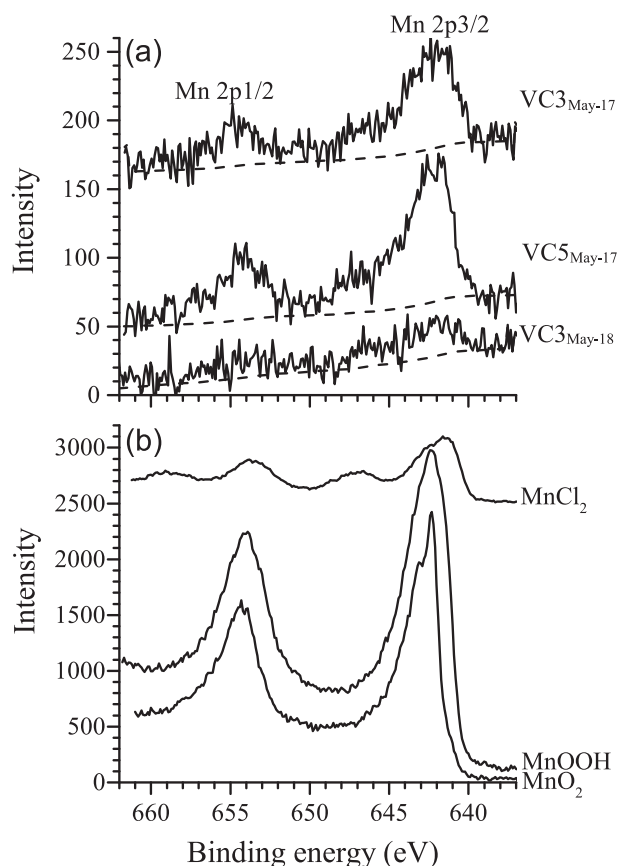
Fig. 5. High-resolution Mn 2p spectra of three SPM samples (a) compared with those of three Mn reference compounds (b). The solid black curves are the experimental data while the dashed curves represent Shirley's background.

the highest Mn loadings (0.43–0.52 %) also exhibited a subtle and broad shoulder at 6561–6562 eV, overall coinciding with the main absorption peaks for the three nanocrystalline phyllomanganate references (triclinic birnessite, hexagonal birnessite, and vernadite; Fig. 6a). This feature clearly pointed to the occurrence of nanocrystalline phyllomanganate phases in these two Mn-rich SPM samples. For LCF-XANES analyses, the Mn references were grouped into four categories, representing silicate-bound Mn, aqueous or organically complexed Mn(II), Mn(II/III) hydroxides, and phyllomanganates, based on the similarities in their XANES spectra (Fig. 6a) and Mn bonding environment (as summarized in Table S5). As described above and shown in Fig. 6a, the reference spectra of each phase group displayed characteristic features that differ distinctively from those in the other groups. Given the high sensitivity of the LCF approach to small but characteristic XAS features (Das et al., 2011), these characteristic features were considered sufficient to allow LCF to statistically differentiate and quantify the contributions from each of the Mn-phase groups and thus provide robust information on both Mn oxidation state and chemistry/mineralogy in the SPM samples. The key LCF-XANES results (Table 2) included: (i) the proportion of silicate-bound Mn was highest (42 %) in the two SPM samples with the lowest Mn loadings ($\leq$0.07 %) and decreased gradually with increasing Mn loadings; (ii) aqueous or organically complexed Mn(II) was a major (36–62 %) Mn fraction throughout although lowest in the two samples with lowest Mn concentrations; and (iii) the fractional amounts of Mn bound to phyllomanganates displayed a strong positive correlation with total Mn loadings, with 17–30 % in the two Mn-richest SPM samples.

The main features in the EXAFS spectra of the SPM samples were overall consistent with those observed for the XANES spectra and the LCF-XANES results. First, the EXAFS spectra of the four SPM samples

with low Mn concentrations, especially those with the lowest concentrations (MC2$_{May-18}$ and TC2$_{May-18}$), overall followed those of biotite and chlorite (Fig. 7). Second, the EXAFS oscillations for the samples with high Mn loadings (VC3$_{May-17}$, VC4$_{May-17}$, and TC4$_{May-17}$) overall followed those of aqueous Mn(II) and Mn(II)-HA. Third, the spectra of the two samples with the highest Mn loadings (and the largest LCF-XANES derived fractional amounts of phyllomanganates) also bore distinctive spectral components arising from phyllomanganates, as reflected by (i) a slight shift of the peaks (indicated by the dashed line in Fig. 7) at k=$\sim$4 Å^{-1} towards the high k region, where the spectra of the phyllomanganate references exhibited strong peaks (k=$\sim$4.2–4.4 Å^{-1}) and (ii) the appearance of a sub-peak at k=$\sim$6.9 Å^{-1} accompanied by strong depression of the peak at k=$\sim$7.5 Å^{-1}(as marked by the two grey bars in Fig. 7), matching with the strongest peak followed by a deep hollow in the same k regions in the spectra of the phyllomanganate references.

Under the guidance of the LCF-XANES results, the FT plots of the Mn K-edge EXAFS spectra (both FT magnitude and real part) for the SPM samples were well reproduced by the contributions from several scattering paths (Mn-O, Mn-Mg, Mn-Si/Al, and Mn-Mn) (SM-3, Fig. S5, Table S7). The fitted structural parameters are reasonable and in line with the LCF-XANES results. For instance, the first FT peak for all SPM samples was contributed significantly by an Mn(II)-O path at 2.15–2.22 Å. The distances agree well with the fitted R_{Mn-O} value for organically complexed and aqueous Mn(II) (Table S8) that were predicted to occur abundantly in all the SPM samples (Table 2). The SPM samples with the low Mn loadings (Mn = 0.05–0.24 %) and high LCF-derived biotite-bound Mn (13–42 %) displayed strong scattering contributions from Mn-Mg and Mn-Si/Al paths at 3.00–3.13 Å and 3.25–3.31 Å (Table S7), which corresponded to the two FT peaks at R + ΔR $\sim$ 2.5 Å and R + ΔR $\sim$ 2.7 Å, respectively (Fig. S5), and matched well with the distances of Mn-Mg (3.09 Å) and Mn-Si/Al (3.29 Å) in biotite (Table S8). The FT plots of the two SPM samples with the highest Mn loadings (and the largest LCF-XANES derived fractional amounts of phyllomanganates), in particular TC2$_{May-18}$, contained a strong peak at R + ΔR $\sim$ 2.5 Å that can be fitted with an Mn-Mn atomic pair at $\sim$ 2.84–2.93 Å, matching well with the distances between the two edge-sharing Mn-Mn coordination within the layers of phyllomanganates (Learman et al., 2011; Liu et al., 2021b; Saratovsky et al., 2009; Webb, 2005) (Table S8).

4.1.4. Estuarine sediments

The sediment cores collected from three sites (S1-S3) in the estuary of the Vörå creek had overall similar and constant concentrations of Al and Fe, fluctuating mainly from 7 % to 8 % and from 4 % to 5 %, respectively (Table S9). The concentrations matched well with those of the SPM samples obtained twice from the above-lying water (Fig. 4b). In contrast, the total concentrations of Mn in the sediment cores, although displaying greater depth and site-dependent variations, were overall much higher than those in the SPM samples (Table S9, Fig. 4b). For the sediment cores at sites S1 and S2, Mn concentrations overall decreased from 1.0 % and 1.2–1.5 % in the uppermost layer(s) to approximately 0.3–0.4 % and 0.5 % in the deepest parts, respectively. The concentrations in the other sediment core remained overall stable (fluctuating around 0.8 %) with no observable depth trend.

The Mn XANES spectra of the uppermost sediment samples from the two innermost sites (S1 and S2) displayed strong absorption maxima at 6562 eV, matching well with those of the phyllomanganate references (Fig. 6b). Also, the EXAFS spectrum of the uppermost sample from site 2 resembled closely the spectra of the phyllomanganate references (Fig. 8). These features provided strong evidence that the Mn pools in the surface sediments at these two sites were strongly dominated by phyllomanganate(s). The XANES spectra of these sediment samples also contained a broad shoulder located at similar energies (6552 eV, Fig. 6b) as the main absorption peak for the Mn(II) references, suggesting a co-existence of small amounts of Mn(II). Given that phyllomanganates can effectively oxidize Mn(II) adsorbed on their vacant sites under alkaline conditions via the comproportionation reaction between the
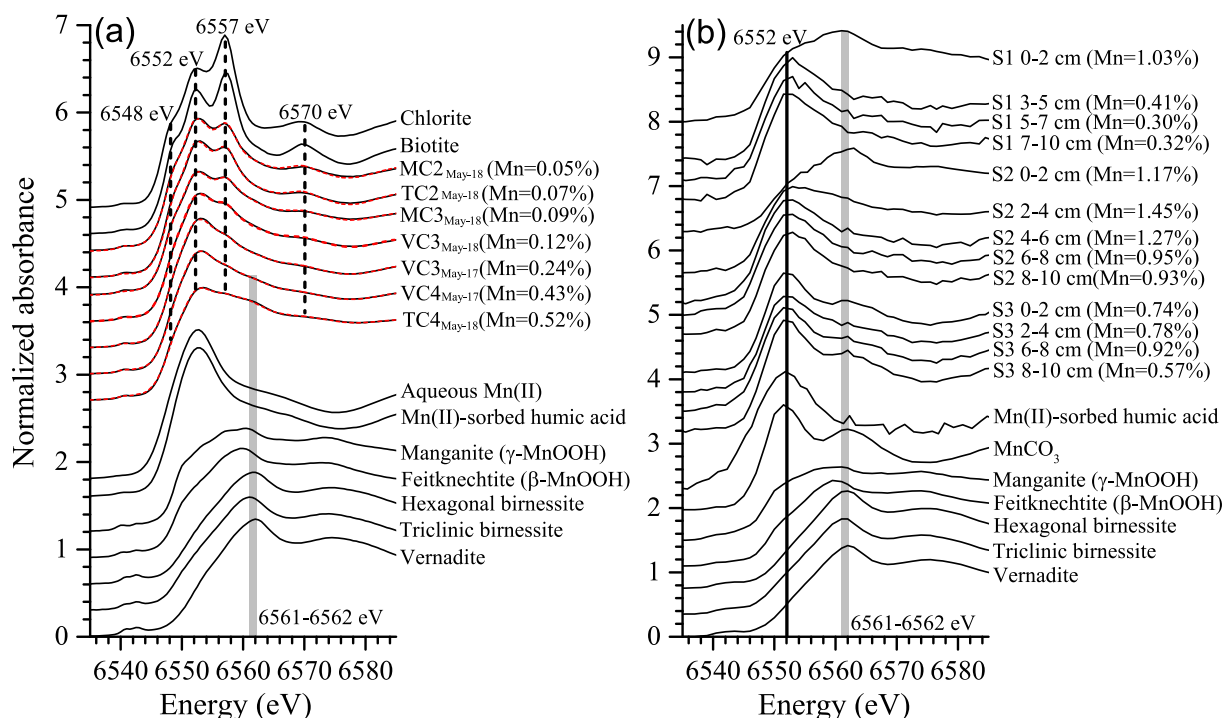
Fig. 6. Normalized Mn K-edge XANES spectra of SPM (a) and sediment (b) samples in comparison with those of reference compounds. Black lines are the experimental data, while the red dashed lines represent the best linear combination fits (Method 1) to the spectra of the SPM samples. Hexagonal birnessite, triclinic birnessite, and vernadite consisted mainly of Mn(IV), with small fractional amounts of Mn(III) and Mn(II). The spectra of the SPM samples and selected references in (a) were recorded on the HXMA beamline at the Canadian Light Source and on the Balder beamline at the MAX-IV, respectively (except the spectrum of aqueous Mn (II) that was collected at the old MAX-lab, detailed information is given in Table S5). The spectra of the sediment samples and selected references in (b) were recorded from the HelXAS beamline at the University of Helsinki. The total concentration of Mn in each of the samples is given in the parentheses.

adsorbed Mn(II) and its surrounding layer Mn(IV) (Hinkle et al., 2016; Wang et al., 2018; Zhao et al., 2016) and that the presence of high levels of divalent cations (e.g., Ca^{2+} and Mg^{2+}) in the porewaters would have competed with Mn(II) for the surface sites on phyllomanganates (Wang et al., 2019), the Mn(II) in these two surface sediments was probably not largely sorbed on coexisting phyllomanganates. Thus, it was most likely largely complexed by organic material (e.g., humic acid), which have been shown to be effective in shielding reduced cations from being oxidized by co-existing phyllomanganates (Yu et al., 2018). The spectra of the deeper sediment layers from these two sites were overall similar to those of Mn(II)-HA or aqueous Mn(II), with a single absorption peak at 6552 eV, pointing to a predominance of organically complexed or mineral-sorbed Mn(II) in the deeper parts of the two cores. However, the spectrum of S2 2–4 cm had an overall broad and flat post-edge between 6552 eV and 6561–6562 eV overlapping with absorption maxima for the Mn(III) and Mn(VI) references and most probably reflecting the occurrence of a mixture of Mn(III) and Mn(IV) phases in this sample.

The XANES spectra of all sediment samples at site S3 displayed a single absorption peak at 6552 eV, indicating a dominance of Mn(II) throughout the core. The spectra for S3 0–2 and S3 8–10 also bore a weak and very broad post-edge shoulder (between ~ 6568 and ~ 6570 eV) with similar shape and energy range as that for the $MnCO_3$. This post-edge feature indicated that large proportions of the Mn occurred as $MnCO_3$.

4.2. Microbial community

The Illumina sequencing generated a total of 23,940,150 reads (minimum 10,928 and maximum 2,442,120 per sample) that generated 33,625 ASVs. Rarefaction analysis of the numbers of ASVs versus the number of generated sequences plateaued for the majority of the samples suggesting microbial taxa were captured (Fig. S6). It should be noted that the 16S rRNA gene PCR primers used in the study were

designed to amplify bacteria and will not include the environmentally important manganese oxidizing fungi or algae (Zhou and Fu, 2020). Non-metric multidimensional scaling (NMDS) analysis of the communities showed a diagonal split between the Vörå creek samples taken in 2017 versus the other samples from 2018 (Fig. S7A) likely due to annual variations. In addition, there was a separation between the MC1, TC1, and VC1 stream samples versus estuary samples on the second axis potentially linked with DOC, iron, and manganese content versus salinity (chloride), respectively. Despite no clear differences in the solid-phase chemical composition (Table S9), the NMDS analysis of the sediment samples also showed a split on the first axis between the 16S rRNA gene ASVs from sites S1 and S2 compared to S3 (Fig. S7B) that was potentially due to core S3 being sampled from the outermost part of the estuary. The samples further split on the second axis between shallower and deeper sediment samples (particularly evident for the S3 samples) likely due to physiochemical changes with sediment depth. One such gradient was oxygenated sediments at the surface altering to sub-oxic and finally anoxic conditions with depth that will select for microbial communities with different metabolic capabilities.

The relative abundances of the 16S rRNA gene amplicon based microbial communities were identified in the water and sediment samples (Fig. S8) and based upon the literature, potential Mn oxidizing genera were identified from the full data set (Fig. 9). The water sample 16S rRNA amplicons were dominated by sequences aligning with Proteobacteria in Munsala and Toby estuaries and on the Vörå estuary sampling occasion in May 2018 and Proteobacteria along with Actinobacteriota in May 2017 (Fig. S8A). The genus *Rhodoferax* was identified as having a high relative abundance in all sampled areas of the Munsala and Toby estuaries along with increasing relative abundances in the Vörå outer estuary on the second sampling occasion (Fig. 9). Although members of the *Rhodoferax* genus have been described as a metabolically diverse group, there is evidence that some strains are capable of Mn (and Fe) oxidation (formerly known as *Albidiferax*; Akob

Table 2

Fractional amounts (in percentage) of Mn phases in SPM samples. The data were quantified by linear combining fitting of the XANES spectra (6530–6590 eV) by two methods (see the main text). The components with fractional amounts ≤ 5 % were not included in the final fit. The component sums were normalized to 100 % (initial range = 99–104 %). Samples are arranged in order of decreasing Mn concentrations. The results should be read primarily in terms of the four major Mn-phase groups whereas percentages for the individual phases (references) within each group should be seen as indicative with possible errors.

	Total Mn concentrations (%)[a]		Silicate-bound Mn	Aqueous or organically complexed Mn(II)		Mn(II/III) hydroxides		Phyllomanganates		R-factor[b]	Concentrations (%) of silicate-bound Mn[c]	Concentrations (%) of secondary Mn(II/III/IV) phases[d]
			Biotite	Mn(II)$_{aq}$	Mn(II)-HA	Hausmannite	Groutite	Vernadite	Triclinic birnessite			
TC4$_{May-18}$	0.52	Method 1	9	8	39		14		30	0.00005	0.05	0.229
		Method 2	10	9	39		19	23		0.00005	0.05	0.218
VC4$_{May-17}$	0.43	Method 1	10		60		9		22	0.00005	0.04	0.133
		Method 2	10		61		12	17		0.00005	0.04	0.125
VC3$_{May-17}$	0.24	Method 1	13		62		14	10		0.00004	0.03	0.058
		Method 2	13		62		14	10		0.00004	0.03	0.058
VC3$_{May-18}$	0.12	Method 1	21		52		18	9		0.00004	0.03	0.032
		Method 2	21		52		18	9		0.00004	0.03	0.032
MC3$_{May-18}$	0.09	Method 1	26	15	27		19		11	0.00007	0.02	0.029
		Method 2	26	16	27		21	9		0.00008	0.02	0.027
TC2$_{May-18}$	0.07	Method 1	42		41		17			0.00013	0.03	0.012
		Method 2	42		41		17			0.00013	0.03	0.012
MC2$_{May-18}$	0.05	Method 1	42		36	14	7			0.00013	0.02	0.011
		Method 2	42		36	14	7			0.00013	0.02	0.004

[a] Total concentrations of Mn in each of the SPM samples determined by ICP-MS.

[b] R-factor = $\sum((data - fit)^2/\sum data^2)$.

[c] Estimated by multiplying the sum of fitted proportions of biotite-bound Mn by the total concentrations of Mn.

[d] Estimated by multiplying the sum of fitted proportions of Mn(II/III) hydroxides and phyllomanganates bound Mn by the total concentrations of Mn.
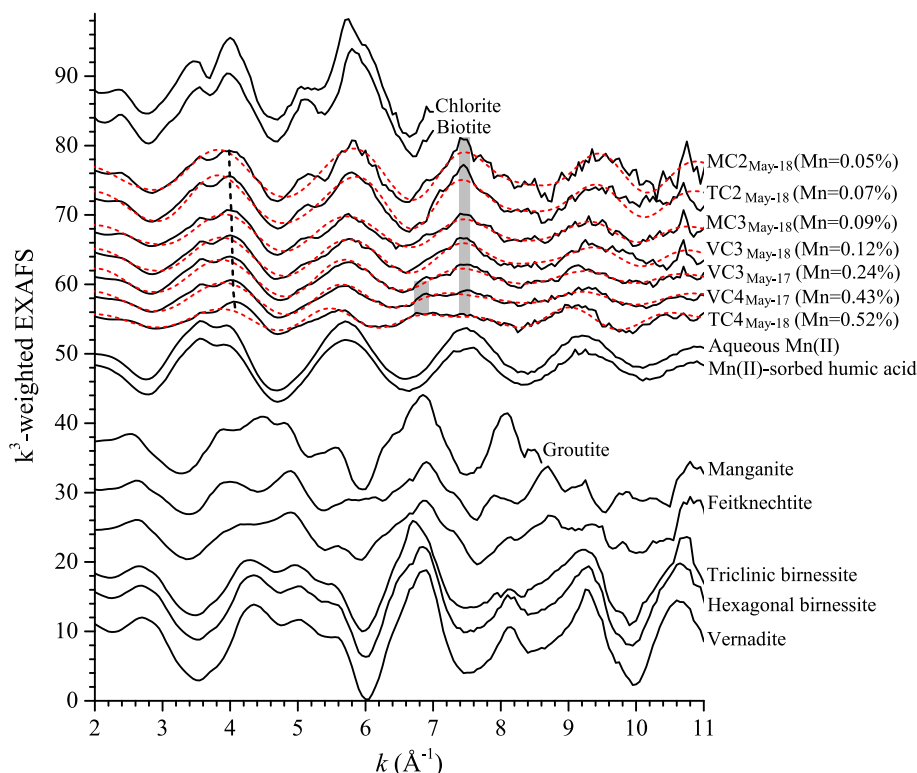
Fig. 7. K³-weighted Mn EXFAS spectra for SPM samples, in comparison with those of reference compounds. Experimental data are shown as black solid lines, while the fits as red dashed lines. The total concentration of Mn in each of the samples is given in the parentheses. Detailed information on the reference materials (e.g., origin and Mn chemical/coordination environments) and their EXAFS spectra (e.g., data source) are summarized in Table S5.
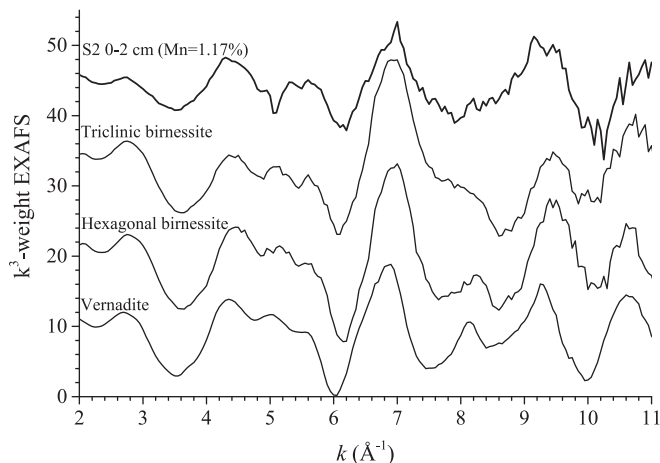

Fig. 8. K³-weighted Mn EXFAS spectrum of the uppermost sediment sample at site S2, in comparison with those of triclinic Na-birnessite, hexagonal birnessite, and vernadite. The spectra of the sediment and references were recorded on the HelXAS beamline using the same experimental set-up.

et al., 2014). In addition, 16S rRNA gene sequences aligning with the *Flavobacterium, Caulobacter*, and *Mycobacterium* genera were identified in almost all water column sample sites and occasions. All these genera are common in aquatic environments, but also include known Mn oxidizer taxa (Akob et al., 2014; Cahyani et al., 2008; Carmichael et al., 2013b; Gregory and Staley, 1982). SEM observation coupled to EDS analysis show that the majority of the microbial cells in the estuarine waters were rod- or filamentous-shaped and attached onto or mixed with inorganic minerals (mainly silicates) (Figs. S9, S10; Table S10).

The 16S rRNA gene amplicon based sediment diversity was greater at the phylum level than the water samples (Fig. S8B) likely due to physiochemical gradients of e.g., oxygen and nutrients selecting for different species. The highest relative abundance of 16S rRNA gene sequences aligning with potential Mn oxidizers belonged to the genus *Leptothrix* (Tebo et al., 2005a), which was identified at all depths at sites 1 and 2 and decreasing below 4 cm at site 3. Further 16S rRNA gene sequences aligning with potential Mn oxidizers in the sediment included the *Blastocatella* genus (Sjöberg et al., 2020) that had a decreasing relative abundance from the surface down to 7 cm depth at site S1 and 4 cm at site S2 (Fig. 10). Once the sediment becomes anoxic at increasing depths in all three sampling sites, Mn cycling may have occurred via anaerobic nitrate-dependent Mn oxidation along with Mn reduction coupled with organic carbon, ammonium, sulfide, or methane oxidation (Wang et al., 2022). Mn reduction may have occurred in the sediments via coupling with organic carbon oxidation by *Shewanella* and *Dechloromonas* species particularly in the deeper site S1 sediments while Mn reduction coupled to methane oxidation may have been mediated by *Candidatus Methanoperedens* that were present in site S3 at all depths but higher relative abundances deeper than 4 cm (Wang et al., 2022 and references therein). However, no candidate anaerobic nitrate-dependent Mn oxidizing taxa were present in the most abundant taxa suggesting they were present at low abundances or that diffusion of the Mn to shallower sediments or the water column where Mn oxidation coupled to the reduction of oxygen may have occurred.

Despite the presence of potential Mn oxidizers in the sediment, 16S rRNA gene amplicon based Picrust analysis of key metabolisms only predicted one Mn oxidation gene (*cotA*, EC 1.16.3.3;(Su et al., 2013) that was present in very low abundances in all sediment samples. However, predicted genes coding for *c*-type cytochromes (e.g., *ccmAEF*), the succinate dehydrogenase complex genes *sdhABCD*, and *icd* isocitrate dehydrogenase all previously identified to play a role in manganese oxidation (Tebo et al., 2005b) were suggested to be present at all three
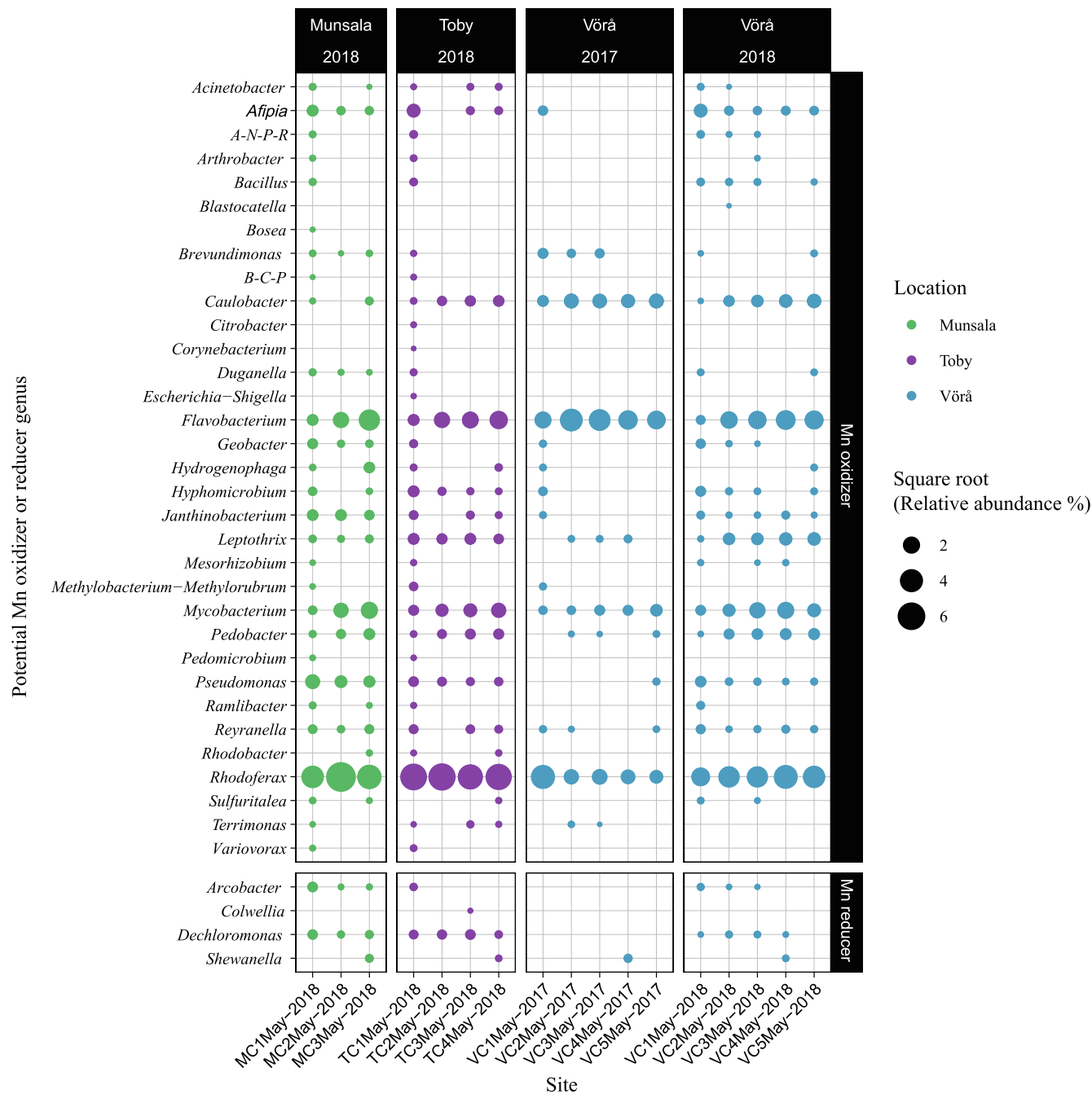
Fig. 9. Relative abundance of microbial genera potentially involved in Mn oxidation and reduction for the surface waters. A-N-P-R, *Allorhizobium-Neorhizobium-Pararhizobium-Rhizobium*; B-C-P, *Burkholderia-Caballeronia-Paraburkholderia*.

sites and depths (Fig. 11). It should be noted that some of these genes encode proteins with various additional functions, e.g., for central metabolism such as the citrate cycle. The genes mediating anaerobic nitrate-dependent Mn oxidation may involve *nar* nitrate reductase, *nir* nitrite reductase, *nor* nitric oxide reductase, and *nos* nitrous oxide reductase (Wang et al., 2022). A number of these genes were predicted to be present with low predicted occurrence at all sites and depths. These low gene relative abundances matched the low relative abundances of the candidate anaerobic nitrate-dependent Mn oxidizing taxa such as *Pseudomonas* or *Acinetobacter*. Methane may have been generated by methanogenesis for which the genes *mtaAB*, *mtbAB*, *mtmB*, and *mttB* were suggested to be present at low relative abundances. While genes coding for aerobic methane oxidation (e.g., *pmoABC*, *amoABC*, and

mmoBCDXYZ) were predicted to be either absent or at very low relative abundances at all three sites and sediment depths, the above-mentioned Mn cycling may have occurred via coupling to anaerobic methane oxidation (that may also have been coupled to sulfate (e.g., *aprAB* and *dsrAB*) that increased in relative abundance with depth), nitrate (described above), and ferric iron reduction (Wang et al., 2022). Genes coding for anaerobic methane oxidation via "reversed methanogenesis" included *hdrABC* present at all three sites and with a trend of increasing relative abundance with depth along with *fwdE/fmdE* that also increased in relative abundance with depth that was particularly evident at site S3.
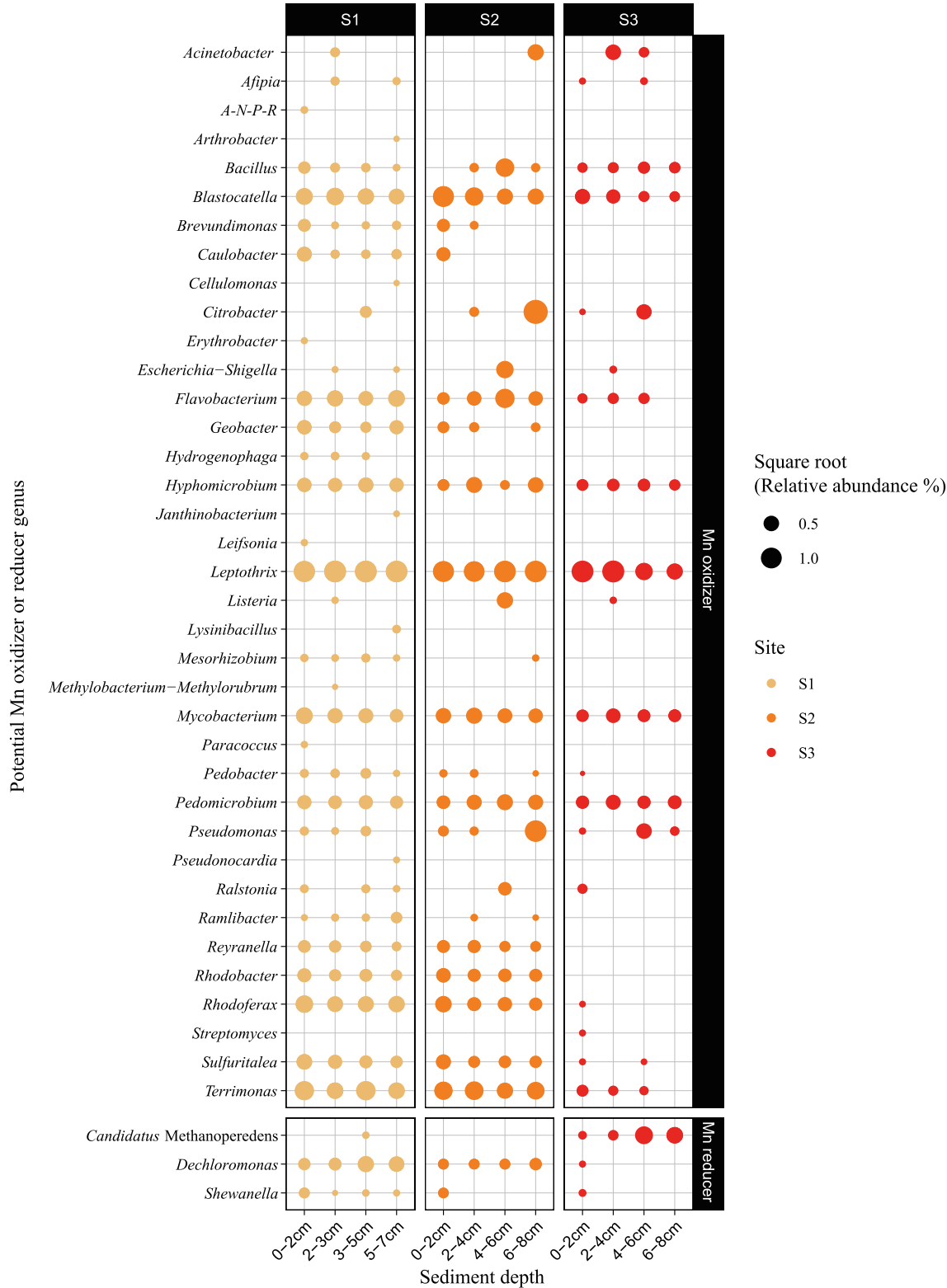
Fig. 10. Relative abundance of microbial genera potentially involved in Mn oxidation and reduction for the sediments.

5. Discussion

5.1. Mn attenuation during the mixing of acidic Mn-rich creek waters and seawater: phases, pathways, and potential roles of Mn-oxidizing microorganisms

The estuarine behavior of Mn (and other metals) exported by the

Vörå creek has previously been studied by applying ultrafiltration (in combination with geochemical modelling) on surface waters and chemical extractions on settling materials collected along a transect from the creek mouth to the outer estuary (Astrom et al., 2012; Nordmyr et al., 2008a; Nordmyr et al., 2008b; Nystrand et al., 2016). These studies found that, in contrast to Fe and Al that are extensively removed in the inner estuary once the acidic creek waters are neutralized, Mn is
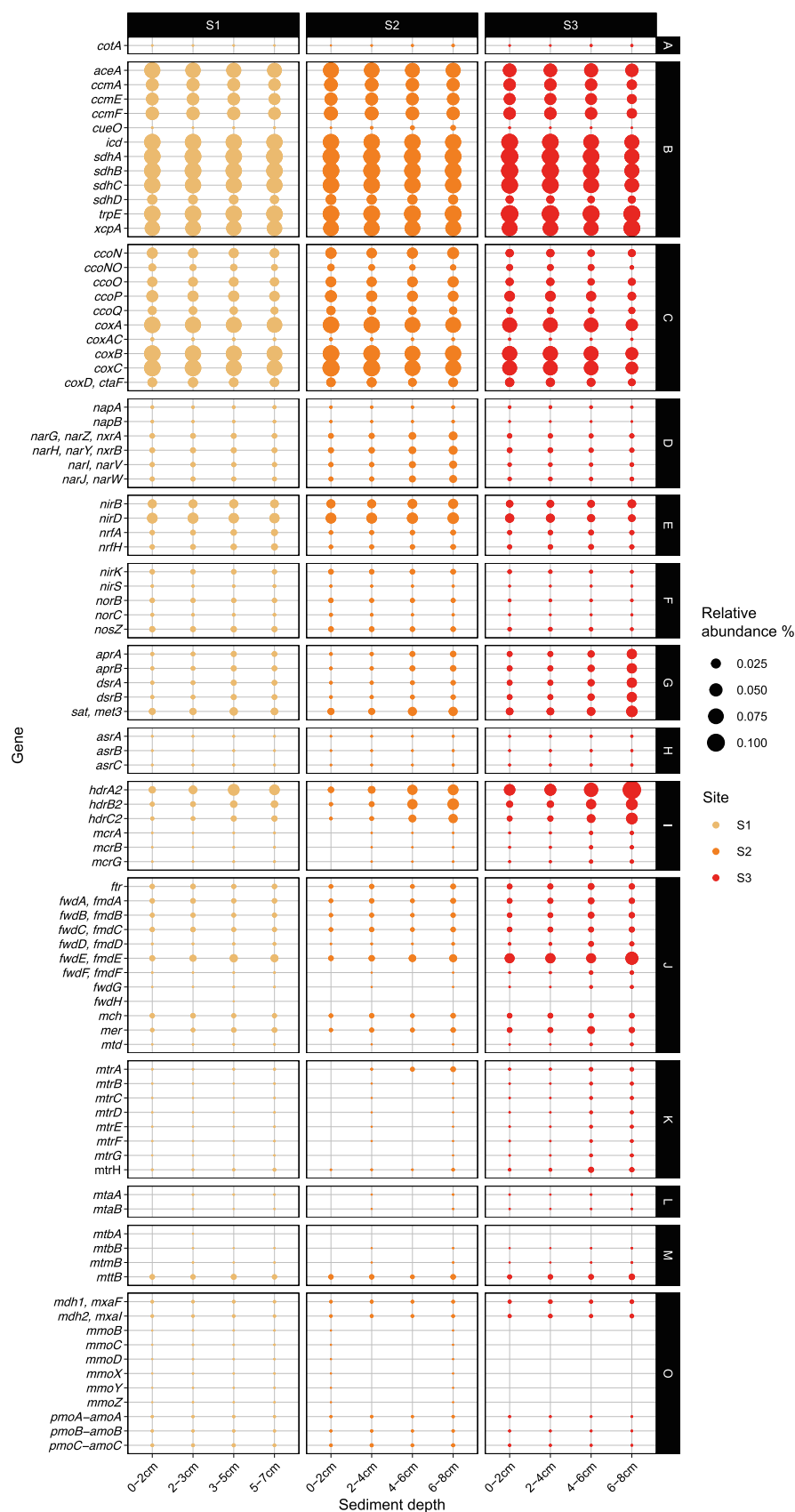
Fig. 11. Predicted key metabolic processes based upon 16S rRNA gene amplicon abundances for the sediments. The categories (right hand side) are: A, Mn oxidation; B, Mn oxidation related (potentially); C, cytochrome *c* oxidase; D, dissimilatory nitrate reduction; E, dissimilatory nitrate reduction, DNRA or ANR; F, denitrification; G, dissimilatory sulfate reduction, sulfate => H₂S; H, sulfite reduction; I, methanogenesis, all; J, methanogenesis, CO₂ => methane; K, methanogenesis, CO₂ => methane or acetate => methane; L, methanogenesis, methanol => methane; M, methanogenesis from other compounds; and O, methane oxidation. I, J, and K can be also reverse methanogenesis.

relatively persistent in the estuarine waters and tends to be transported to the central/outer parts of the estuarine mixing zone, before being episodically transformed into particulate phases. During the two sampling campaigns in 2017 and 2018, similar features were observed. First, the dissolved Mn loads decreased at much slower rates as compared to the dissolved loads of Al and Fe (Fig. 4b) and second, both the bulk dried materials and the outermost layers of the wet SPM samples obtained from the central/outer parts of the estuary were loaded with overall higher, and often strongly elevated, levels of Mn compared to those from the inner estuary (Fig. 4b; Table 1). Such features were also evident for the other two estuaries, suggesting that Mn behavior and attenuation in the estuarine mixing zones of the estuaries was governed by robust processes. Although being successively diluted by the brackish seawater in a manner similar to the dissolved Mn fraction, the > 0.1 μm fraction of Mn remained overall stable across the estuarine mixing zone of the Vörå estuary, in sharp contrast to those of Fe and Al that strongly decreased (Fig. 4b). This feature further pointed to an active and continuous transformation of dissolved Mn fractions to the particulate and colloidal Mn fractions during the successive mixing of the Mn-rich creek waters and brackish seawaters.

Based on the LCF-XANES results (Table 2) the sums of the proportions of Mn(II/III) hydroxides plus phyllomanganates were significantly correlated with the Mn loadings (method 1: $r_{Spearman} = 0.72$, $p < 0.08$, $n = 7$; method 2 $r_{Spearman} = 0.82$, $p < 0.03$, $n = 7$), which means that both the relative and absolute amounts of these Mn phases strongly increased as the Mn concentrations increased. These features suggested that the removal of Mn down the estuary was largely regulated by the oxidation of Mn and subsequent formation of Mn(II/III) hydroxides and phyllomanganates, as suggested in previous studies based on the extractability of Mn by hydroxylamine-hydrochloride in Mn-enriched settling materials collected in the Vörå estuary (Astrom et al., 2012; Nordmyr et al., 2008a). In addition to these phases (referred to as "MnOx"), organically complexed Mn(II) and/or aqueous Mn(II) potentially representing both dissolved and loosely surface-sorbed Mn(II) species were also modelled to occur abundantly in the SPM samples, in particular those from the outer parts of the estuaries. Although these Mn (II) phases did not increase proportionally with the total Mn loadings and thus were not the main drivers for the removal of Mn, they still act as important vectors transferring labile Mn(II) from the water columns to the estuarine seafloor, particularly in the outer parts of the estuaries.

The LCF-XANES analysis also revealed abundant silicate-bound Mn (as biotite) in the SPM samples with the lowest Mn loadings (Fig. 6a; Table 2). As a common and Mn(II)-rich primary mineral, the biotite fraction in the SPM is derived from erosion of the till and fine-grained sediments, which are the dominating soil types in the catchments and contain abundant fine-grained biotite (and other sheet silicates) that are easily mobilized in the extensively ditched catchments (Astrom and Björklund, 1997). The relative proportions of biotite-bound Mn in the SPM samples correlated inversely with the total Mn loadings, explained by increasing contributions of other phases at higher loadings. However, the concentrations of this silicate-bound Mn varied only slightly (0.02–0.05 %, Table 2), indicating an overall low but rather constant deposition of detrital Mn throughout the estuaries. It is also worth noting that the Mn XANES spectra of the biotite reference and the SPM samples with the largest LCF-derived percentages of silicate-bound Mn (TC2$_{May-18}$ and MC2$_{May-18}$) closely resembled one of the Mn XANES spectral components (extracted from a large high-resolution Mn XANES dataset of a Holocene-aged sediment section) that was interpreted to represent the input of detrital aluminosilicate-bound Mn to the northern Gotland Basin (Lenz et al., 2014). In that study, it was also found that the concentrations of this detrital Mn fraction remain overall low and constant throughout the whole sediment section deposited during approximately 8000–4000 cal. yr BP. Thus, it appears that the estuaries and deep basins of the Baltic Sea receive an overall constant input of detrital Mn fractions, dominated by biotite containing Mn mainly in divalent state.

Abiotic oxidation of Mn(II) by dissolved O_2 is kinetically very slow,

even under circumneutral-alkaline pH conditions (Diem and Stumm, 1984; Morgan, 2005). However, a growing body of studies show that this process can be greatly enhanced in the presence of mineral surfaces (Hu, 2023; Inoué et al., 2019; Jung, 2021; Lan, 2017, 2021; Liu et al., 2021a; Madden and Hochella, 2005; Wang, 2015). The enhancement is believed to be driven by the inner-sphere adsorption of both dissolved Mn(II) and O_2 onto mineral surfaces, which not only increase the local concentrations/interactions of Mn(II) and O_2, but also reduce the activation energy of electron transfer from surface-sorbed Mn(II) to O_2 (Junta and Hochella, 1994; Lan et al., 2017; Liu et al., 2021a). This could ultimately promote the oxidation of Mn(II) via facilitating (i) direct interfacial electron transfer between adsorbed Mn(II) and O_2 species that are in close contact with each other ("the interfacial catalytic pathway") or (ii) indirect electron transfer from adsorbed Mn(II) species to the "cathodic and remote" surface sites with O_2 molecules through the conduction bands of semiconducting minerals ("the electrochemical pathway") (Hu et al., 2023; Inoué et al., 2019; Lan et al., 2017; Liu et al., 2021a). Since the electrochemical pathway does not require a physical contact between surface-sorbed Mn(II) and O_2 species, it was considered to be more effective in promoting the oxidation of surface-sorbed Mn(II) on the semiconducting minerals (Lan et al., 2017). Owing to their ubiquitous occurrences and large active surfaces with semiconductive properties, Fe (hydr-)oxides are expected to play a crucial role in surface-catalyzed oxidation of Mn(II) in various (near-)surface environments. A previous Fe XAS study on the SPM samples from the mouths of the Toby and Vörå creeks showed that ferrihydrite was the only observable Fe-oxide phase exported by the creeks (Yu et al., 2015), consistent with a strong predominance of such a phase together with organically complexed Fe(III) in boreal streams/rivers and recipient estuaries (Herzog et al., 2017; Herzog et al., 2020; Sundman et al., 2014; Sundman et al., 2013). Previous experimental studies show that, similar to other Fe (hydr-)oxides (e.g., hematite, manganite, goethite, and lepidocrocite), ferrihydrite promotes Mn(II) oxidation in aerated and weakly acidic to alkaline solutions (pH 6.5–8) that results in heterogeneous growth of different Mn(II/III) hydroxides (e.g., manganite, feiknechtite, groutite, and hausmannite) on the surfaces of ferrihydrite particles (Han et al., 2016; Junta and Hochella, 1994; Lan et al., 2021; Lan et al., 2017; Wang et al., 2015). However, these experimental studies were conducted by reacting pure ferrihydrite particles with relatively high levels of Mn(II) (2–24 mM) that are two to four orders of magnitude higher than the concentrations of dissolved Mn(II) in the estuarine waters in this study. Another study showed that, although the theoretical minimum value of dissolved Mn(II) for activating electrochemical Mn(II) oxidation on ferrihydrite is 0.0125 mM, the actual occurrence of significant electrochemical oxidation of Mn on ferrihydrite requires much higher Mn(II) concentrations (e.g., >4 mM) under their experimental conditions (Lan et al., 2017). Indeed, a recent experimental study (Jung et al., 2021) found that the reactions of pure ferrihydrite with 0.1 mM Mn in both deionized water and artificial seawater resulted in minimal to negligible Mn oxidation, even with the constant exposure to lamp light that significantly promote the surface-catalyzed Mn(II) oxidation by hematite and goethite (Lan et al., 2017). In the studied estuaries, the ferrihydrite particles are expected to be largely aggregated with and/or coated by organics (consisting of negatively charged organic macromolecules with poor abilities in shuttling electrons) and newly formed insulating Al hydroxides once the acidic Al- and OM-rich creek waters are neutralized in the inner estuaries. These processes are likely to strongly suppress inner-sphere adsorption of Mn(II) and O_2 as well as their electron transfer on the active surface sites of ferrihydrite particles as demonstrated experimentally (Ma et al., 2020), which in combination with the low dissolved Mn(II) concentrations should greatly inhibit surface-catalyzed Mn oxidation on the surface of these particles via either the interfacial or electrochemical pathways. It is thus likely that ferrihydrite particles, despite occurring abundantly in the estuarine waters, had a negligible role in catalyzing the Mn(II) oxidation in the estuaries.

Microorganisms (bacterial and fungi) catalyze Mn(II) oxidation (e.g., Nealson et al., 1988; Tebo et al., 2004) and thus, are commonly invoked as a key biological factor controlling the formation of Mn hydroxides in various environments (Bargar et al., 2009; Dick et al., 2009; Miller et al., 2012; Sjöberg et al., 2021; Tebo et al., 2004; Tebo et al., 2005a). During the sampling campaigns, a large variety of potential Mn oxidizing genera were present in the surface waters of the three estuaries (Fig. 9). Even though *Rhodoferax* was the most abundant of these genera in the estuarine waters, its relative abundance did not exhibit any clear or consistent estuary-wide trends. In contrast, the relative abundances of *Flavobacterium, Caulobacter, Mycobacterium, and Pedobacter*, although being slightly less abundant, increased down the estuaries (Fig. 9) and thus were more likely to play a role in Mn(II) oxidation. This was supported by the increase in pH down the estuaries as circumneutral pH conditions strongly favor both abiotic and microbially-mediated Mn(II) oxidation (Bargar, 2005; Miyata et al., 2007; Tebo et al., 2005a) and an early study showing that the average Mn oxidation state of the solid phases (initially dominated by hausmannite) produced by the *Bacillus* species cultivated with pH 7.5 seawater and 2 μM Mn(II) increased from approximately 2.7 to 3.8 within four weeks (Hastings and Emerson, 1986). The mechanisms whereby microorganisms mediate/promote Mn(II) oxidation is generally believed to proceed via two slightly different pathways (both involving two sequential one-electron steps), during which dissolved Mn(II) is (i) rapidly oxidized to Mn(II/III) hydroxides (e.g., hausmannite or MnOOH) that subsequently disproportionate to Mn(IV) and Mn(II) and (ii) directly oxidized to Mn(VI) phases with enzyme-complexed Mn(III) as functional intermediate phases (Tebo et al., 2004). Although there is increasing evidence from laboratory-based cultivation experiments that microbially-mediated Mn(II) oxidation directly produces poorly-crystalline phyllomanganates with hexagonal sheet symmetry similar to vernadite or hexagonal birnessite, the phases hausmannite and groutite (MnOOH) are also occasionally reported to be the dominant Mn solid-phases in the cultures of *Bacillus*, *Cladosporium*, and *Nevskia* species (Hastings and Emerson, 1986; Sjöberg et al., 2021). Considering that the presence of relatively low Mn(II) concentrations (e.g., <500 μM) at weakly-alkaline pH could result only in structural transformations of phyllomanganates from hexagonal to triclinic layer symmetry (Bargar, 2005; Zhao et al., 2016), groutite indicated to occur in the SPM samples was most probably not a secondary product of Mn(II)-induced alterations of the phyllomanganates (in the studied estuaries being reacted only with < 5 μM Mn(II); Fig. 4b), but was produced by Mn(II) oxidation mediated by the aforementioned potential Mn oxidizing genera.

5.2. Early-diagenesis and recycling of Mn

One of the notable features for the sediment cores from the two innermost sites (S1 and S2) in the Vörå estuary was that their surfaces (0–2 cm) contained abundant Mn (1.0–1.2 %, Table S9) that primarily existed as vernadite- or birnessite-like phases (Fig. 6b and 8). The Mn concentrations in these two surface sediments were much higher than those of the SPM samples obtained from the same sites (VC3 and VC4). A likely explanation was that the SPM samples were collected on only two short occasions and thus, cannot represent the long-term Mn loadings recorded in the sediments. On the other hand, the Mn concentrations in the two sediments fell within the ranges of those in the settling materials collected previously over three consecutive years from the upper and lower parts of the water column close to site S1 (Nordmyr et al., 2008a). The Mn in these settling materials, in particular those with the highest Mn concentrations (up to 2.6 %), was nearly quantitatively extracted by hydroxylamine-hydrochloride but only marginally with sodium pyrophosphate (generally less than 10 %) targeting organically complexed elements. These results do not match the LCF-XANES results of the SPM samples from the same site (VC3) with approximately 50–60 % of organically bound Mn(II) (Table 2). Since the SPM samples contained much lower Mn concentrations (0.12–0.24 %) than the settling materials

collected previously, this discrepancy could simply reflect a dilution effect. That is, occasional massive Mn oxidation and subsequent formation of MnOx, which seems not to have occurred during the samplings of the SPM samples, occurred during the sampling of the settling material, thus decreasing the relative size of organically-complexed Mn(II). Collectively, these features and results provided evidence that the total Mn loads on the seafloor at these two sites were dominated by vernadite/birnessite-like phases that were derived largely from the water column, in particular during periods when massive Mn oxidation occurred. The Mn XANES data further indicated that the deposited MnOx phases were rapidly reduced within the upper 3–4 cm of the sediment cores and converted to organically complexed or loosely surface-sorbed Mn(II) species (Fig. 6b). These processes were possibly mediated by potential Mn reducers (e.g., *Dechloromonas* and *Shewanella*; Fig. 10) and should produce abundant upward diffusing Mn flux that was partly re-oxidized to MnOx in the surface sediments and partly released to the overlaying bottom waters (Widerlund and Ingri, 1996). The oxidation of the upward Mn flux in the surface sediments can be catalyzed by pre-existing MnOx phases and the potential Mn oxidizers (Fig. 10) by using dissolved O_2 and nitrate as electron acceptors, further contributing to the enrichments of MnOx in the surface sediments at these two sites.

In the sediment at site S3, in contrast, MnOx did not occur but there was strong indication of a $MnCO_3$ phase in particular in the uppermost sample (Fig. 6b), in line with previous detection of this mineral in sediments in this estuary (Yu et al., 2016). The estuarine waters are, however, undersaturated with respect to $MnCO_3$ (Yu et al., 2016). Furthermore, the sediments at this site contained most of the potential Mn-oxidizer genera (in particular those possibly involving in Mn oxidation in the water column), with similar abundances, as well as similar predicted functional genes and cytochrome *c* oxidases potentially linked to Mn oxidation, as the sediments at the other two sites (Figs. 10 and 11). Taken together, these features suggested that the removal of Mn at site S3 was not due to deposition of $MnCO_3$ but most likely MnOx as at the other sites. Compared to the other sites, site S3 was located further out in the estuary and thus, had a lower sedimentation rate, a deeper water depth, and a higher input of both phytoplankton-derived organics and low-molecular-weight terrestrial humic substances. All these could have contributed to a rapid and near-quantitative reduction of MnOx and subsequent formation of $MnCO_3$ close to the water–sediment interface at this site.

5.3. Anaerobic oxidation of methane and potential roles of Mn (hydr-) oxides

(Near-)surface sediments in estuarine and coastal systems of the Baltic Sea and other marginal seas are frequently reported to contain appreciable amounts of porewater methane and sustain relatively high rates of methanogenesis (Egger et al., 2015; Myllykangas et al., 2019; Myllykangas et al., 2020; Perner et al., 2022; Purkamo et al., 2022; Rooze et al., 2016; Żygadłowska et al., 2023), resulting in the emission of large diffusive methane fluxes to the overlying waters and atmosphere (Cotovicz et al., 2021; Dutta et al., 2015; Zang et al., 2022; Żygadłowska et al., 2023). Also, the concentrations and estimated oxidation rates of porewater methane in these systems are found to increase considerably offshore (Myllykangas et al., 2019; Myllykangas et al., 2020; Purkamo et al., 2022). Although sulfate and methane porewater data were not obtained for the sediment cores, functional genes putatively involved in sulfate reduction and methane metabolism (methanogenesis and reverse methanogenesis) were suggested to be present throughout these cores, and displayed constant estuary-wide patterns and depth-related trends that comply well with the results of the previous studies (Fig. 11). First, the relative abundances of most of the predicted functional genes for sulfate reduction and methane metabolism increased gradually with depth, pointing to increasing metabolic potentials for these processes favored by the development of more strictly anoxic conditions in deeper

sediment layers. Since most of the functional genes for methane metabolism (sub-groups I-K, Fig. 11) could be involved in both methanogenesis and reverse methanogenesis (potentially mediated by the same microbes or syntrophic couplings as previously found (Beaulieu et al., 2019; Maltby et al., 2016), the concomitant increase in the relative abundance of these functional genes with those for sulfate reduction might reflect, in addition to increasing rates of methanogenesis, on-going sulfate-dependent anaerobic oxidation of methane (AOM) that can be mediated by a syntrophic consortium of anaerobic methane oxidizing archaea and sulfate-reducing bacteria (Boetius et al., 2000; McGlynn et al., 2015; Michaelis et al., 2002). Second, the predicted relative abundance of these functional genes overall increased down estuary from site S1 to S3, indicating stronger metabolic activities of sulfur and methane in the sediments of the outer estuary. This trend might be attributed to that the sediments in the outer estuary (i) receive higher inputs of phytoplankton-derived (and easily-degradable) organic fractions favoring remineralization processes (e.g., sulfate reduction and methanogenesis) and (ii) hold higher levels of sulfate that could further sustain higher rates of sulfate reduction and co-linked AOM (Myllykangas et al., 2020).

It is increasingly recognized that Mn and Fe (hydr-)oxides may not only act as direct electron acceptors for methanotrophs to oxidize methane (Bar-Or et al., 2017; Leu et al., 2020; Liu et al., 2020; Rooze et al., 2016; Sujith et al., 2014), but also may support sulfate-dependent AOM through a "cryptic" sulfur cycle, during which reduced sulfur species are constantly re-oxidized back to sulfate sustaining sulfate-dependent AOM under sulfate-starved conditions (Egger et al., 2017; Holmkvist et al., 2011; Mostovaya et al., 2021; Su et al., 2019). Given the relative low availability of sulfate due to fresh-brackish conditions as well as the co-occurrence of abundant MnOx phases and relatively high numbers of predicted genes related to sulfate reduction and methane metabolism in the near-surface sediments at sites S1 and S2, the MnOx phases and their redox-cycling might contribute to AOM in the sediments at these sites either via (i) a direct coupling of AOM and MnOx reduction mediated by e.g., *Candidatus Methanoperedens* (Fig. 10) that has been suggested to be potentially involved in AOM coupled to Fe and/

or Mn reduction in other coastal settings (Wallenius et al., 2021; Żygadłowska et al., 2023) or (ii) indirectly via supporting sulfate-dependent AOM. In addition, the presence of approximately 3–4 cm sediment layers with abundant MnOx at these sites could, in addition to Fe (hydr-)oxides, slow down the depletion/exhaustion of porewater sulfate, as (i) MnOx phases are highly reactive towards sulfides and can rapidly oxidize them back to sulfate and (ii) Mn-reducing bacteria could suppress the activities of sulfate-reducing bacteria by outcompeting limited organic substrates. These processes could push down the sulfate-methane transition zone, allowing for a more efficient sulfate-dependent AOM in the studied estuaries. This has implications for mitigating the upward fluxes of methane from estuarine and coastal sediments, where the sulfate-methane transition zones have been found to be typically shallow (Egger et al., 2015; Myllykangas et al., 2019; Myllykangas et al., 2020) and have significantly migrated upwards due to intensified anthropogenic eutrophication during the past decades (Egger et al., 2015; Wallenius et al., 2021).

5.4. A conceptual model of Mn behavior in estuaries receiving acidic Mn-rich fresh waters

The results of this study provided strong evidence that Mn export, attenuation, and seaward transport in the three creeks-estuaries are governed by common phases and similar biogeochemical processes/factors, and thus represent a robust fundamental system. As conceptualized in Fig. 12, this system displays three distinct zones with characteristic Mn phases and biogeochemical processes. Once acidic Mn-rich creek water enters the estuary and thus is mixed with seawater (zone 1), Mn-containing silicates derived from soil erosion in the catchments settle along with organically-complexed Mn(II). The source of the organic matter is widespread peat and humus-rich soils in the catchments, and the mixing with Mn, derived from the AS soils, occur either within-creek or in zone 1. In the central and outer estuary (zones 2 and 3), the remaining Mn continues to be removed with settling silicates and, to a greater extent as organically-complexed Mn(II) and microbially-derived MnOx-phases like phyllomanganates and groutite. While
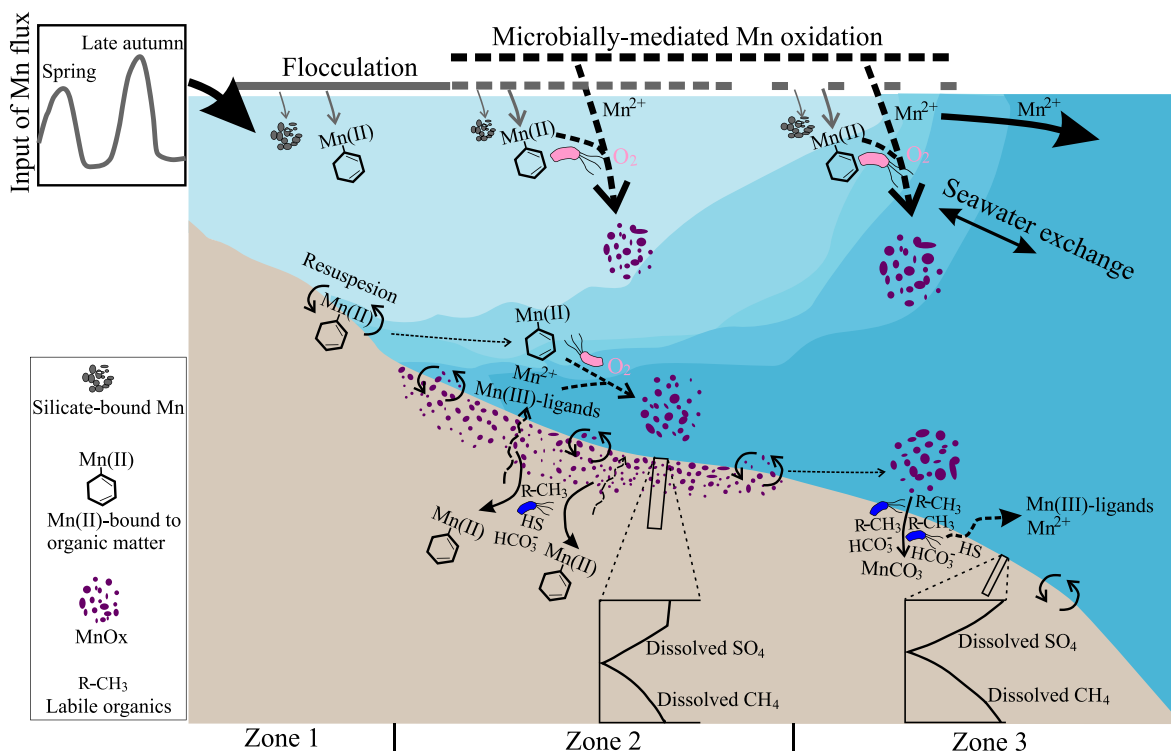

Fig. 12. Conceptualized model of Mn input, removal, cycling, and lateral transport in a typical acid sulfate soil impacted estuary.

predictions based upon 16S rRNA gene amplicons require laboratory confirmation by e.g., enrichment cultures, potential Mn-oxidizing microorganisms identified included *Flavobacterium*, *Caulobacter*, *Mycobacterium*, and *Pedobacter*. On the seafloor within zone 2, the deposited MnOx are largely preserved as phyllomanganates in surface sediments, but reduced and converted to surface-sorbed Mn(II) phases (presumably complexed with organic matter) at deeper layers (>3–4 cm). The preserved MnOx phases might suppress the reduction of sulfate in the surface sediments, thereby pushing down the methane sulfate transition zone that is typically shallow in estuarine sediments. In contrast, the deposited MnOx at zone 3 are immediately reduced at the water–sediment interface and converted most likely to Mn carbonate. These reduction processes could produce abundant reduced Mn species (e.g., aqueous Mn(II) and ligands complexed Mn(III)), part of which can diffuse into the overlying waters and be transported down estuary. Considering the short residence time of estuarine surface waters and the relatively high Mn concentrations observed for the surface waters in the outermost part of the estuaries, large fractions of the estuarine Mn loads are expected to reach open coastal areas, in particular during high flow conditions. These estuarine Mn loads, together with diffusive Mn efflux from the estuarine sediments, will contribute to Mn shuttling and interlinked biogeochemical processes over the shallow coast areas and associated deep basins.

6. Conclusions

This study focused on Mn biogeochemistry in estuaries that are episodically fed by very acidic and Mn-rich waters from oxidizing sulfide-bearing sediments (acid sulfate soils) in the catchments. The Mn behavior was found to be complex and dynamic, including temporal variations as well as down-estuary and down-core changes in Mn concentrations, redox state, and solid-phase speciation. However, the identified features were similar in all three studied creeks-estuaries, which indicated robust fundamental processes controlling Mn and allowed us to propose a conceptual model of Mn behavior in these kinds of settings. The microbiological characterization identified several bacteria that may be central in the oxidation of Mn in the water column, leading to formation of Mn (hydr-)oxides (dominated by phyllomanganates) that ultimately settle and eventually are reduced at various rates in the surface layers of the sediments. The latter mechanism is proposed to affect the methane dynamics in the sediments.

On coastal areas worldwide geological materials with the potential to produce acidic Mn-enriched waters that ultimately reach estuaries are widespread. This include, in particular, coastal acid sulfate soils which were the focus of this study but also sulfide-enriched bedrock and mining activities in areas with sulfide mineralization producing acid mine drainage. The identified Mn behavior, including complex and dynamic processes over both spatial and temporal scales across the entire estuarine zone, is thus relevant for a number of situations that occur globally. On a broader scale the identified Mn reactions have implications for Mn transport to oceans and for an increased efficiency of sulfate-dependent AOM in estuarine and coastal systems. An extension of the study should include manganese oxidizing fungi and algae that are important in many settings as well as determination of sulfate and methane in sediment porewaters.

Data availability

Data are available through Mendeley Data at: https://doi.org/10.17632/kr2t7cty7n.1.

Declaration of competing interest

The authors declare that they have no known competing financial interests or personal relationships that could have appeared to influence the work reported in this paper.

Appendix A. Supplementary material

The supplementary material includes deconvolution and interpretation of high-resolution XPS spectra (Text SM-1); procedures for the preparation of Mn reference materials (Text SM-2); details of EXAFS shell fitting (Text SM-3); sample information, DNA concentrations, and number of reads for surface water and sediment samples (Tables S1 and S2); list of taxa and genes potentially involved in Mn oxidation or reduction (Tables S3 and S4); list of Mn reference compounds (Table S5); hydrochemistry of the surface waters (Table S6); EXAFS shell fitting results for SPM samples (Table S7); local structure of selected Mn reference compounds (Table S8); physio-chemical properties of the sediment cores (Table S9); SEM-EDS results (Table S10); photos of the sediment cores (Fig. S1); wide-scan and high-resolution XPS spectra (Figs. S2, S3, and S4); EXAFS shell fitting results for SPM samples (Fig. S5); rarefaction curves and NMDS analysis of the 16S rRNA gene sequencing data (Figs. S6 and S7); stacked bar of 16S rRNA gene amplicons at the level of phylum and family (Fig. S8); and SEM images of bacterial cells/biofilms (Figs. S9 and S10).

Supplementary material to this article can be found online at https://doi.org/10.1016/j.gca.2023.12.004.

References

Akob, D.M., et al., 2014. Identification of Mn(II)-oxidizing bacteria from a low-pH contaminated former uranium mine. Appl Environ Microbiol 80 (16), 5086–5097.

Allard, S., Gutierrez, L., Fontaine, C., Croué, J.-P., Gallard, H., 2017. Organic matter interactions with natural manganese oxide and synthetic birnessite. Sci Total Environ 583, 487–495.

Andriesse, W., Van Mensvoort, M., 2006. Acid sulfate soils: distribution and extent. Encyclopedia of Soil Science 1, 14–19.

Astrom, M.E., et al., 2010. Lanthanoid behaviour in an acidic landscape. Geochim. Cosmochim. Acta 74 (3), 829–845.

Astrom, M.E., et al., 2012. Attenuation of rare earth elements in a boreal estuary. Geochim. Cosmochim. Acta 96, 105–119.

Astrom, M.E., et al., 2018. Sources, transport and sinks of beryllium in a coastal landscape affected by acidic soils. Geochim. Cosmochim. Acta 232, 288–302.

Astrom, M., Björklund, A., 1995. Impact of acid sulfate soils on stream water geochemistry in western Finland. J. Geochem. Explor. 55 (1–3), 163–170.

Astrom, M., Björklund, A., 1997. Geochemistry and acidity of sulphide-bearing postglacial sediments of western Finland. Environ. Geochem. Health. 19 (4), 155–164.

Balaguer, J., Koch, F., Hassler, C., Trimborn, S., 2022. Iron and manganese co-limit the growth of two phytoplankton groups dominant at two locations of the Drake Passage. Commun Biol 5 (1), 207.

Bargar, J.R., 2005. Biotic and abiotic products of Mn(II) oxidation by spores of the marine Bacillus sp. strain SG-1. Am. Mineral. 90 (1), 143–154.

Bargar, J.R., et al., 2009. Structural characterization of terrestrial microbial Mn oxides from Pinal Creek. AZ. Geochim. Cosmochim. Acta 73 (4), 889–910.

Bar-Or, I., et al., 2017. Iron-Coupled Anaerobic Oxidation of Methane Performed by a Mixed Bacterial-Archaeal Community Based on Poorly Reactive Minerals. Environ Sci Technol. 51 (21), 12293–12301.

Beaulieu, J.J., DelSontro, T., Downing, J.A., 2019. Eutrophication will increase methane emissions from lakes and impoundments during the 21st century. Nat Commun 10 (1), 1375.

Boetius, A., et al., 2000. A marine microbial consortium apparently mediating anaerobic oxidation of methane. Nature 407 (6804), 623–626.

Boman, A., Åström, M., Fröjdö, S., 2008. Sulfur dynamics in boreal acid sulfate soils rich in metastable iron sulfide—The role of artificial drainage. Chem. Geol. 255 (1–2), 68–77.

Boman, A., Fröjdö, S., Backlund, K., Åström, M.E., 2010. Impact of isostatic land uplift and artificial drainage on oxidation of brackish-water sediments rich in metastable iron sulfide. Geochim. Cosmochim. Acta 74 (4), 1268–1281.

Browning, T.J., Achterberg, E.P., Engel, A., Mawji, E., 2021. Manganese co-limitation of phytoplankton growth and major nutrient drawdown in the Southern Ocean. Nat Commun 12 (1), 884.

Cahyani, V.R., Murase, J., Ishibashi, E., Asakawa, S., Kimura, M., 2008. Phylogenetic positions of Mn2+-oxidizing bacteria and fungi isolated from Mn nodules in rice field subsoils. Biol. Fertil. Soils. 45 (4), 337–346.

Carmichael, M.J., Carmichael, S.K., Santelli, C.M., Strom, A., Bräuer, S.L., 2013a. Mn (II)-oxidizing bacteria are abundant and environmentally relevant members of ferromanganese deposits in caves of the upper Tennessee River Basin. Geomicrobiology Journal 30 (9), 779–800.

Carmichael, M.J., Carmichael, S.K., Santelli, C.M., Strom, A., Bräuer, S.L., 2013b. Mn(II)-oxidizing Bacteria are Abundant and Environmentally Relevant Members of Ferromanganese Deposits in Caves of the Upper Tennessee River Basin. Geomicrobiol. J. 30 (9), 779–800.

Chaput, D.L., et al., 2019. Mn oxide formation by phototrophs: Spatial and temporal patterns, with evidence of an enzymatic superoxide-mediated pathway. Sci Rep 9 (1), 18244.

Chaput, D.L., Hansel, C.M., Burgos, W.D., Santelli, C.M., 2015. Profiling microbial communities in manganese remediation systems treating coal mine drainage. Appl. Environ. Microbiol. 81 (6), 2189–2198.

Charette, M.A., et al., 2016. Coastal ocean and shelf-sea biogeochemical cycling of trace elements and isotopes: lessons learned from GEOTRACES. Philos Trans A Math Phys Eng Sci 374 (2081), 20160076.

Chorover, J., Amistadi, M.K., 2001. Reaction of forest floor organic matter at goethite, birnessite and smectite surfaces. Geochim. Cosmochim. Acta 65 (1), 95–109.

Cotovicz Jr., L.C., et al., 2021. Greenhouse gas emissions (CO(2) and CH(4)) and inorganic carbon behavior in an urban highly polluted tropical coastal lagoon (SE, Brazil). Environ Sci Pollut Res Int 28 (28), 38173–38192.

Das, S., Hendry, M.J., Essilfie-Dughan, J., 2011. Transformation of two-line ferrihydrite to goethite and hematite as a function of pH and temperature. Environ Sci Technol. 45 (1), 268–275.

Dellwig, O., et al., 2010. A new particulate Mn–Fe–P-shuttle at the redoxcline of anoxic basins. Geochim. Cosmochim. Acta 74 (24), 7100–7115.

Destouni, G., Hannerz, F., Prieto, C., Jarsjö, J., Shibuo, Y., 2008. Small unmonitored near-coastal catchment areas yielding large mass loading to the sea. Glob. Biogeochem. Cycles. 22 (4).

Dick, G.J., et al., 2009. Enzymatic microbial Mn(II) oxidation and Mn biooxide production in the Guaymas Basin deep-sea hydrothermal plume. Geochim. Cosmochim. Acta 73 (21), 6517–6530.

Diem, D., Stumm, W., 1984. Is dissolved Mn2+ being oxidized by O2 in absence of Mn-bacteria or surface catalysts? Geochim. Cosmochim. Acta 48 (7), 1571–1573.

Douglas, G.M., et al., 2020. PICRUSt2 for prediction of metagenome functions. Nat. Biotechnol. 38 (6), 685–688.

Dutta, M.K., Mukherjee, R., Jana, T.K., Mukhopadhyay, S.K., 2015. Biogeochemical dynamics of exogenous methane in an estuary associated to a mangrove biosphere; The Sundarbans, NE coast of India. Mar. Chem. 170, 1–10.

Egger, M., et al., 2015. Iron-mediated anaerobic oxidation of methane in brackish coastal sediments. Environ Sci Technol. 49 (1), 277–283.

Egger, M., et al., 2017. Iron oxide reduction in methane-rich deep Baltic Sea sediments. Geochim. Cosmochim. Acta 207, 256–276.

EN, D., 1997. Water Analysis-Guidelines for the Determination of Total Organic Carbon (TOC) and Dissolved Organic Carbon (DOC).

Estes, E.R., Andeer, P.F., Nordlund, D., Wankel, S.D., Hansel, C.M., 2016. Biogenic manganese oxides as reservoirs of organic carbon and proteins in terrestrial and marine environments. Geobiology 15 (1), 158–172.

Fairley, N., 2009. CasaXPS Manual 2.3.15: CasaXPX Processing Software for XPS Spectra. Casa Software.

Fernandes, S.O., et al., 2015. Anaerobic nitrification–denitrification mediated by Mn-oxides in meso-tidal sediments: Implications for N$_2$ and N$_2$O production. J. Mar. Syst. 144, 1–8.

Finnish Field Drainage Center, 2001. Salaojitus Suomessa. 1959–2000 (Helsinki. 127 p., in Finnish).

Flynn, E.D., Catalano, J.G., 2019. Reductive transformations of layered manganese oxides by small organic acids and the fate of trace metals. Geochim. Cosmochim. Acta 250, 149–172.

Grangeon, S., Lanson, B., Miyata, N., Tani, Y., Manceau, A., 2010. Structure of nanocrystalline phyllomanganates produced by freshwater fungi. Am. Mineral. 95 (11–12), 1608–1616.

Gregory, E., Staley, J.T., 1982. Widespread distribution of ability to oxidize manganese among freshwater bacteria. Appl Environ Microbiol. 44 (2), 509–511.

Han, X., et al., 2016. Lepidocrocite-catalyzed Mn(II) oxygenation by air and its effect on the oxidation and mobilization of As(III). Appl. Geochem. 72, 34–41.

Hansel, C.M., Zeiner, C.A., Santelli, C.M., Webb, S.M., 2012. Mn(II) oxidation by an ascomycete fungus is linked to superoxide production during asexual reproduction. Proc Natl Acad Sci U S a. 109 (31), 12621–12625.

Hastings, D., Emerson, S., 1986. Oxidation of manganese by spores of a marine Bacillus: kinetic and thermodynamic considerations. Geochim. Cosmochim. Acta 50 (8), 1819–1824.

Hermans, M., et al., 2019. Impact of natural re-oxygenation on the sediment dynamics of manganese, iron and phosphorus in a euxinic Baltic Sea basin. Geochim. Cosmochim. Acta 246, 174–196.

Herndon, E.M., Martínez, C.E., Brantley, S.L., 2014. Spectroscopic (XANES/XRF) characterization of contaminant manganese cycling in a temperate watershed. Biogeochemistry 121 (3), 505–517.

Herzog, S.D., Persson, P., Kritzberg, E.S., 2017. Salinity Effects on Iron Speciation in Boreal River Waters. Environ Sci Technol. 51 (17), 9747–9755.

Herzog, S.D., Persson, P., Kvashnina, K., Kritzberg, E.S., 2020. Organic iron complexes enhance iron transport capacity along estuarine salinity gradients of Baltic estuaries. Biogeosciences 17 (2), 331–344.

Hinkle, M.A., Flynn, E.D., Catalano, J.G., 2016. Structural response of phyllomanganates to wet aging and aqueous Mn (II). Geochim. Cosmochim. Acta 192, 220–234.

Holmkvist, L., Ferdelman, T.G., Jørgensen, B.B., 2011. A cryptic sulfur cycle driven by iron in the methane zone of marine sediment (Aarhus Bay, Denmark). Geochim. Cosmochim. Acta 75 (12), 3581–3599.

Honkanen, A.-P., et al., 2019. Johann-type laboratory-scale x-ray absorption spectrometer with versatile detection modes. Rev. Sci. Instrum. 90 (3), 033107.

Hu, S., et al., 2023. Hematite-mediated Mn(II) abiotic oxidation under oxic conditions: pH effect and mineralization. J Colloid Interface Sci 636, 267–278.

Hugerth, L.W., et al., 2014. DegePrime, a program for degenerate primer design for broad-taxonomic-range PCR in microbial ecology studies. Appl Environ Microbiol 80 (16), 5116–5123.

Hyun, J.-H., et al., 2017. Manganese and iron reduction dominate organic carbon oxidation in surface sediments of the deep Ulleung Basin. East Sea. Biogeosciences 14 (4), 941–958.

Inoué, S., Yasuhara, A., Ai, H., Hochella, M.F., Murayama, M., 2019. Mn(II) oxidation catalyzed by nanohematite surfaces and manganite/hausmannite core-shell nanowire formation by self-catalytic reaction. Geochim. Cosmochim. Acta 258, 79–96.

Jensen, L.T., et al., 2020. A comparison of marine Fe and Mn cycling: U.S. GEOTRACES GN01 Western Arctic case study. Geochim. Cosmochim. Acta 288, 138–160.

Jensen, M.M., Thamdrup, B., Rysgaard, S., Holmer, M., Fossing, H., 2003. Rates and regulation of microbial iron reduction in sediments of the Baltic-North Sea transition. Biogeochemistry 65, 295–317.

Jilbert, T., Slomp, C.P., 2013. Iron and manganese shuttles control the formation of authigenic phosphorus minerals in the euxinic basins of the Baltic Sea. Geochim. Cosmochim. Acta 107, 155–169.

Johnson, K., et al., 2015. Towards a mechanistic understanding of carbon stabilization in manganese oxides. Nat Commun. 6, 7628.

Jones, M.E., et al., 2018. Manganese-Driven Carbon Oxidation at Oxic-Anoxic Interfaces. Environ Sci Technol.

Jung, H., et al., 2021. Photocatalytic oxidation of dissolved Mn(II) on natural iron oxide minerals. Geochim. Cosmochim. Acta 312, 343–356.

Junta, J.L., Hochella Jr, M.F., 1994. Manganese (II) oxidation at mineral surfaces: A microscopic and spectroscopic study. Geochim. Cosmochim. Acta 58 (22), 4985–4999.

Lan, S., et al., 2017. Mechanisms of Mn(II) catalytic oxidation on ferrihydrite surfaces and the formation of manganese (oxyhydr)oxides. Geochim. Cosmochim. Acta 211, 79–96.

Lan, S., et al., 2021. Kinetics of Mn(II) adsorption and catalytic oxidation on the surface of ferrihydrite. Sci Total Environ. 791, 148225.

Learman, D.R., et al., 2011. Coupled biotic–abiotic Mn(II) oxidation pathway mediates the formation and structural evolution of biogenic Mn oxides. Geochim. Cosmochim. Acta 75 (20), 6048–6063.

Lee, J.-M., et al., 2021. Changing chemistry of particulate manganese in the near- and far-field hydrothermal plumes from 15°S East Pacific Rise and its influence on metal scavenging. Geochim. Cosmochim. Acta 300, 95–118.

Lenstra, W.K., et al., 2019. The shelf-to-basin iron shuttle in the Black Sea revisited. Chem. Geol. 511, 314–341.

Lenstra, W.K., et al., 2022. Sediments as a Source of Iron, Manganese, Cobalt and Nickel to Continental Shelf Waters (Louisiana, Gulf of Mexico). Front. Mar. Sci. 9.

Lenz, C., Behrends, T., Jilbert, T., Silveira, M., Slomp, C.P., 2014. Redox-dependent changes in manganese speciation in Baltic Sea sediments from the Holocene Thermal Maximum, An EXAFS, XANES and LA-ICP-MS study. Chem. Geol. 370, 49–57.

Lenz, C., Jilbert, T., Conley, D.J., Slomp, C.P., 2015. Hypoxia-driven variations in iron and manganese shuttling in the Baltic Sea over the past 8 kyr. Geochem. Geophys. Geosystems. 16 (10), 3754–3766.

Leu, A.O., et al., 2020. Anaerobic methane oxidation coupled to manganese reduction by members of the Methanoperedenaceae. ISME J. 14 (4), 1030–1041.

Leven, A., Vlassopoulos, D., Kanematsu, M., Goin, J., O'Day, P.A., 2018. Characterization of manganese oxide amendments for in situ remediation of mercury-contaminated sediments. Environ Sci Process Impacts. 20 (12), 1761–1773.

Liu, S., et al., 2019. Benzene promotes microbial Fe(III) reduction and flavins secretion. Geochim. Cosmochim. Acta 264, 92–104.

Liu, W., et al., 2020. Reduction of methane emissions from manganese-rich constructed wetlands: Role of manganese-dependent anaerobic methane oxidation. Chem. Eng. J. 387.

Liu, Y., et al., 2021b. Photo-stimulated anoxic reduction of birnessite (δ-MnO2) by citrate and its fine structural responses: Insights on a proton-promoted photoelectron transfer process. Chem. Geol. 561.

Liu, J., Inoué, S., Zhu, R., He, H., Hochella, M.F., 2021a. Facet-specific oxidation of Mn (II) and heterogeneous growth of manganese (oxyhydr)oxides on hematite nanoparticles. Geochim. Cosmochim. Acta 307, 151–167.

Ma, D., Wu, J., Yang, P., Zhu, M., 2020. Coupled manganese redox cycling and organic carbon degradation on mineral surfaces. Environ Sci Technol. 54 (14), 8801–8810.

Macdonald, B.C.T., et al., 2007. Discharge of weathering products from acid sulfate soils after a rainfall event, Tweed River, eastern Australia. Appl. Geochem. 22 (12), 2695–2705.

Madden, A.S., Hochella, M.F., 2005. A test of geochemical reactivity as a function of mineral size: Manganese oxidation promoted by hematite nanoparticles. Geochim. Cosmochim. Acta 69 (2), 389–398.

Mäkinen, J., Saaranen, V., 1998. Determination of post-glacial land uplift from the three precise levellings in Finland. J. Geod. 72 (9), 516–529.

Maltby, J., Sommer, S., Dale, A.W., Treude, T., 2016. Microbial methanogenesis in the sulfate-reducing zone of surface sediments traversing the Peruvian margin. Biogeosciences 13 (1), 283–299.

Manceau, A., Marcus, M.A., Grangeon, S., 2012. Determination of Mn valence states in mixed-valent manganates by XANES spectroscopy. Am. Mineral. 97 (5–6), 816–827.

Mattsson, T., Kortelainen, P., Räike, A., Lepistö, A., Thomas, D.N., 2015. Spatial and temporal variability of organic C and N concentrations and export from 30 boreal rivers induced by land use and climate. Sci Total Environ. 508, 145–154.

McGlynn, S.E., Chadwick, G.L., Kempes, C.P., Orphan, V.J., 2015. Single cell activity reveals direct electron transfer in methanotrophic consortia. Nature 526 (7574), 531–535.

Michaelis, W., et al., 2002. Microbial reefs in the Black Sea fueled by anaerobic oxidation of methane. Science 297 (5583), 1013–1015.

Miller, A., et al., 2012. Biogenic Mn oxide minerals coating in a subsurface granite environment. Chem. Geol. 322, 181–191.

Miyata, N., Tani, Y., Sakata, M., Iwahori, K., 2007. Microbial manganese oxide formation and interaction with toxic metal ions. J. Biosci. Bioeng. 104 (1), 1–8.

Morgan, J.J., 2005. Kinetics of reaction between O2 and Mn (II) species in aqueous solutions. Geochim. Cosmochim. Acta 69 (1), 35–48.

Mosley, L.M., Fitzpatrick, R.W., Palmer, D., Leyden, E., Shand, P., 2014. Changes in acidity and metal geochemistry in soils, groundwater, drain and river water in the Lower Murray River after a severe drought. Sci Total Environ. 485, 281–291.

Mostovaya, A., Wind-Hansen, M., Rousseau, P., Bristow, L.A., Thamdrup, B., 2021. Sulfate- and iron-dependent anaerobic methane oxidation occurring side-by-side in freshwater lake sediment. Limnol. Oceanogr. 67 (1), 231–246.

Myllykangas, J.-P., Hietanen, S., Jilbert, T., 2019. Legacy Effects of Eutrophication on Modern Methane Dynamics in a Boreal Estuary. Estuaries and Coasts. 43 (2), 189–206.

Myllykangas, J.-P., Rissanen, A.J., Hietanen, S., Jilbert, T., 2020. Influence of electron acceptor availability and microbial community structure on sedimentary methane oxidation in a boreal estuary. Biogeochemistry 148 (3), 291–309.

Nichols, D., Greenhill, A., Shadbolt, C., Ross, T., McMeekin, T., 1999. Physicochemical parameters for growth of the sea ice bacteria Glaciecola punicea ACAM 611Tand Gelidibacter sp. Strain IC158. Appl Environ Microbiol. 65 (8), 3757–3760.

Nordmyr, L., Osterholm, P., Astrom, M., 2008a. Estuarine behaviour of metal loads leached from coastal lowland acid sulphate soils. Mar Environ Res. 66 (3), 378–393.

Nordmyr, L., Åström, M., Peltola, P., 2008b. Metal pollution of estuarine sediments caused by leaching of acid sulphate soils. Estuar. Coast. Shelf Sci. 76 (1), 141–152.

Nystrand, M.I., Österholm, P., Yu, C., Åström, M., 2016. Distribution and speciation of metals, phosphorus, sulfate and organic material in brackish estuary water affected by acid sulfate soils. Appl. Geochem. 66, 264–274.

Oksanen, J., et al., 2019. Vegan: community ecology package (version 2.5-6). The Comprehensive R Archive Network.

Owings, S.M., et al., 2021. Differential manganese and iron recycling and transport in continental margin sediments of the Northern Gulf of Mexico. Mar. Chem. 229.

Perner, M., et al., 2022. Environmental changes affect the microbial release of hydrogen sulfide and methane from sediments at Boknis Eck (SW Baltic Sea). Front Microbiol. 13, 1096062.

Post, J.E., 1999. Manganese oxide minerals: Crystal structures and economic and environmental significance. Proc Natl Acad Sci U S a. 96, 3447–3454.

Purkamo, L., et al., 2022. Impact of submarine groundwater discharge on biogeochemistry and microbial communities in pockmarks. Geochim. Cosmochim. Acta 334, 14–44.

R Core Team, 2019. R: A Language and Environment for Statistical Computing R Foundation for Statistical Computing. Austria, Vienna.

Ramstedt, M., Andersson, B.M., Shchukarev, A., Sjöberg, S., 2004. Surface Properties of Hydrous Manganite (γ-MnOOH). A Potentiometric, Electroacoustic, and X-ray Photoelectron Spectroscopy Study. Langmuir 20 (19), 8224–8229.

Rautio, L., Ilvessalo, H., 1998. Miljöns tillstånd i västra Finland. Västra Finlands miljöcentral, Österbottens förbund och Etelä-Pohjanmaan liitto (296 pp., in Swedish and Finnish).

Ravel, B., Newville, M., 2005. ATHENA, ARTEMIS, HEPHAESTUS: data analysis for X-ray absorption spectroscopy using IFEFFIT. J. Synchrotron Radiat. 12 (4), 537–541.

Rooze, J., Egger, M., Tsandev, I., Slomp, C.P., 2016. Iron-dependent anaerobic oxidation of methane in coastal surface sediments: Potential controls and impact. Limnol. Oceanogr. 61 (S1), S267–S282.

Santelli, C.M., et al., 2010. Promotion of Mn (II) oxidation and remediation of coal mine drainage in passive treatment systems by diverse fungal and bacterial communities. Appl. Environ. Microbiol. 76 (14), 4871–4875.

Santelli, C.M., Webb, S.M., Dohnalkova, A.C., Hansel, C.M., 2011. Diversity of Mn oxides produced by Mn(II)-oxidizing fungi. Geochim. Cosmochim. Acta 75 (10), 2762–2776.

Santelli, C.M., Chaput, D.L., Hansel, C.M., 2014. Microbial communities promoting Mn (II) oxidation in Ashumet Pond, a historically polluted freshwater pond undergoing remediation. Geomicrobiology Journal 31 (7), 605–616.

Saratovsky, I., Gurr, S.J., Hayward, M.A., 2009. The Structure of manganese oxide formed by the fungus Acremonium sp. strain KR21-2. Geochim. Cosmochim. Acta 73 (11), 3291–3300.

Seidel, L., et al., 2022. Weakened resilience of benthic microbial communities in the face of climate change. ISME Communications. 2 (1), 1–9.

Shchukarev, A., Boily, J.-F., Felmy, A.R., 2007. XPS of Fast-Frozen Hematite Colloids in NaCl Aqueous Solutions I. Evidence for the Formation of Multiple Layers of Hydrated Sodium and Chloride Ions Induced by the 001 Basal Plane. J. Phys. Chem. C 111 (49), 18307–18316.

Sjöberg, S., et al., 2020. Microbiomes in a manganese oxide producing ecosystem in the Ytterby mine, Sweden: impact on metal mobility. FEMS Microbiol Ecol. 96 (11).

Sjöberg, S., et al., 2021. Microbe-Mediated Mn Oxidation—A Proposed Model of Mineral Formation. Minerals. 11 (10).

Straub, D., et al., 2020. Interpretations of environmental microbial community studies are biased by the selected 16S rRNA (gene) amplicon sequencing pipeline. Front. Microbiol. 11, 550420.

Su, J., et al., 2013. CotA, a multicopper oxidase from Bacillus pumilus WH4, exhibits manganese-oxidase activity. PLoS One. 8 (4), e60573.

Su, G., et al., 2019. Manganese/iron-supported sulfate-dependent anaerobic oxidation of methane by archaea in lake sediments. Limnol. Oceanogr. 65 (4), 863–875.

Sujith, P.P., Gonsalves, M.J.B.D., Rajkumar, V., Miriam Sheba, V., 2014. Manganese cycling and its implication on methane related processes in the Andaman continental slope sediments. Mar. Pet. Geol. 58, 254–264.

Sunda, W.G., Kieber, D.J., 1994. Oxidation of humic substances by manganese oxides yields low-molecular-weight organic substrates. Nature 367 (6458), 62–64.

Sundman, A., Karlsson, T., Persson, P., 2013. An experimental protocol for structural characterization of Fe in dilute natural waters. Environ Sci Technol. 47 (15), 8557–8564.

Sundman, A., Karlsson, T., Laudon, H., Persson, P., 2014. XAS study of iron speciation in soils and waters from a boreal catchment. Chem. Geol. 364, 93–102.

Tan, W.-F., et al., 2008. Determination of the point-of-zero charge of manganese oxides with different methods including an improved salt titration method. Soil Sci. 173 (4), 277–286.

Tebo, B.M., et al., 2004. Biogenic manganese oxides: properties and mechanisms of formation. Annu. Rev. Earth Planet. Sci. 32, 287–328.

Tebo, B.M., Johnson, H.A., McCarthy, J.K., Templeton, A.S., 2005a. Geomicrobiology of manganese(II) oxidation. Trends Microbiol. 13 (9), 421–428.

Tebo, B.M., Johnson, H.A., McCarthy, J.K., Templeton, A.S., 2005b. Mn (II) oxidation by fungi. Trends Microbiol. 9 (13), 421–428.

Tessin, A., et al., 2020. Arctic Continental Margin Sediments as Possible Fe and Mn Sources to Seawater as Sea Ice Retreats: Insights From the Eurasian Margin. Glob. Biogeochem. Cycles. 34 (8).

Thamdrup, B., Canfield, D.E., 1996. Pathways of carbon oxidation in continental margin sediments off central Chile. Limnol. Oceanogr. 41 (8), 1629–1650.

Villalobos, M., Toner, B., Bargar, J., Sposito, G., 2003. Characterization of the manganese oxide produced by pseudomonas putida strain MnB1. Geochim. Cosmochim. Acta 67 (14), 2649–2662.

Virtasalo, J.J., Österholm, P., Kotilainen, A.T., Åström, M.E., 2020. Enrichment of trace metals from acid sulfate soils in sediments of the Kvarken Archipelago, eastern Gulf of Bothnia. Baltic Sea. Biogeosciences. 17 (23), 6097–6113.

Wallenius, A.J., Dalcin Martins, P., Slomp, C.P., Jetten, M.S.M., 2021. Anthropogenic and Environmental Constraints on the Microbial Methane Cycle in Coastal Sediments. Front Microbiol. 12, 631621.

Wang, X., et al., 2015. The Presence of Ferrihydrite Promotes Abiotic Formation of Manganese (Oxyhydr)oxides. Soil Sci Soc Am J. 79 (5), 1297–1305.

Wang, X., et al., 2022. Anaerobic microbial manganese oxidation and reduction: a critical review. Sci Total Environ. 153513.

Wang, Q., Yang, P., Zhu, M., 2018. Structural transformation of birnessite by fulvic acid under anoxic conditions. Environ Sci Technol. 52 (4), 1844–1853.

Wang, Q., Yang, P., Zhu, M., 2019. Effects of metal cations on coupled birnessite structural transformation and natural organic matter adsorption and oxidation. Geochim. Cosmochim. Acta 250, 292–310.

Webb, S.M., 2005. Structural characterization of biogenic Mn oxides produced in seawater by the marine bacillus sp. strain SG-1. Am. Mineral. 90 (8–9), 1342–1357.

Webb, S.M., Tebo, B., Barger, J., 2005. Structural influences of sodium and calcium ions on the biogenic manganese oxides produced by the marine Bacillus sp., strain SG-1. Geomicrobiol. J. 22 (3–4), 181–193.

Widerlund, A., Ingri, J., 1996. Redox cycling of iron and manganese in sediments of the Kalix River estuary, Northern Sweden. Aquat. Geochem. 2, 185–201.

Wu, Z., et al., 2020. Transformation of Ni-containing birnessite to tectomanganate: Influence and fate of weakly bound Ni(II) species. Geochim. Cosmochim. Acta 271, 96–115.

Yaraghi, N., et al., 2020. Impacts of gold mine effluent on water quality in a pristine sub-Arctic river. J. Hydrol. 589, 125170.

Yli-Halla, M., 1997. Classification of acid sulphate soils of Finland according to Soil Taxonomy and the FAO/Unesco legend. Agric. Food Sci. 6 (3), 247–258.

Yu, C.X., et al., 2015. Iron behavior in a northern estuary: Large pools of non-sulfidized Fe(II) associated with organic matter. Chem. Geol. 413, 73–85.

Yu, C.X., et al., 2016. Manganese accumulation and solid-phase speciation in a 3.5m thick mud sequence from the estuary of an acidic and Mn-rich creek, northern Baltic Sea. Chem. Geol. 437, 56–66.

Yu, C., et al., 2018. A cryogenic XPS study of Ce fixation on nanosized manganite and vernadite: Interfacial reactions and effects of fulvic acid complexation. Chem. Geol. 483, 304–311.

Yu, Q., Sasaki, K., Tanaka, K., Ohnuki, T., Hirajima, T., 2012. Structural factors of biogenic birnessite produced by fungus Paraconiothyrium sp. WL-2 strain affecting sorption of Co2+. Chem. Geol. 310–311, 106–113.

Yuan, S., et al., 2018. Mechanisms of electron transfer from structrual Fe(II) in reduced nontronite to oxygen for production of hydroxyl radicals. Geochim. Cosmochim. Acta 223, 422–436.

Zang, K., et al., 2022. Methane emission via sediment and water interface in the Bohai Sea. China. J Environ Sci (china) 114, 465–474.

Zhang, Y., et al., 2019. A novel manganese oxidizing bacterium-Aeromonas hydrophila strain DS02: Mn (II) oxidization and biogenic Mn oxides generation. J. Hazard. Mater. 367, 539–545.

Zhang, J., McKenna, A.M., Zhu, M., 2021. Macromolecular Characterization of Compound Selectivity for Oxidation and Oxidative Alterations of Dissolved Organic Matter by Manganese Oxide. Environ Sci Technol. 55 (11), 7741–7751.

Zhao, H., et al., 2016. Redox Reactions between Mn(II) and Hexagonal Birnessite Change Its Layer Symmetry. Environ Sci Technol. 50 (4), 1750–1758.

Zhou, Z., et al., 2022. High-throughput sequencing reveals the main drivers of niche-differentiation of bacterial community in the surface sediments of the northern South China sea. Mar. Environ. Res. 178, 105641.

Zhou, H., Fu, C., 2020. Manganese-oxidizing microbes and biogenic manganese oxides: characterization, Mn (II) oxidation mechanism and environmental relevance. Reviews in Environmental Science and Bio/technology. 19, 489–507.

Żygadłowska, O.M., et al., 2023. Pathways of methane removal in the sediment and water column of a seasonally anoxic eutrophic marine basin. Front. Mar. Sci. 10.